# Exploring Cosmic-ray acceleration in the Galactic realm

---

David I. Jones
BSc(Hons)


School of Chemistry & Physics, University of Adelaide

October 20, 2009

*A thesis submitted in total fulfillment of the requirements for the degree of Doctor of Philosophy*

NOTE:
Statements of authorship appear in the print copy of
the thesis held in the University of Adelaide Library.

# 8

# Discovery of a SNR at the edge of the Sgr B2 cloud

This chapter is based on a manuscript which is currently in preparation for submission to the Astrophysical Journal and is entitled: *Non-thermal emission near Sgr B2: A new Supernova remnant in the Galactic centre?*

## 8.1 Abstract

We report the discovery of a non-thermal radio source, which we name the Southern Complex, located to the south of the Sagittarius B2 (Sgr B2) giant molecular cloud. From radio continuum observations between 1384 and 8640 MHz with the Very Large Array and the Australia Telescope Compact Array, we find a spectral index for the source of $\alpha = -0.7 \pm 0.1$ between 1384 and 2368 MHz, and $\alpha = -0.4 \pm 0.1$ between 2368 and 8640 MHz. We have used archival ATCA data to search for 1720 MHz OH maser emission towards the Sgr B2 region. Although no maser emission was observed, we have used line-subtracted continuum data to uncover a low-level extension to the south west of the main source.

Using archival 50 ks *XMM-Newton* data we have discovered an extended X-ray source which is coincident with the southwesterly extension found in the 1720 MHz continuum data. The line-of-sight column density towards the Southern Complex source, at $12.5^{+2.8}_{-1.0} \times 10^{22}$ cm$^{-2}$, is high. Spectral modeling of this source is best described with a 2-component thermal plasma spectrum model plus Gaussian line. The first thermal component has a temperature of $kT > 10$ keV, and together with a strong 6.4 keV line is probably associated with Galactic center component. The second component, which has a temperature of $kT \sim 0.15^{+0.08}_{-0.03}$ keV, together with the presence of the 1.8 keV Si line, suggests that this source could be a $\sim$ 3000 year old SNR.

Although there is not a positional coincidence of radio and X-ray emission, the high column density in the region leads to an X-ray emissivity which is not high enough to produce an unambiguous detection. Together with the X-ray source being located at the same projected position as a large gradient in $NH_3$ density, we argue that the X-ray and radio emission belong to the same source. On the basis of the newly discovered X-ray source, it is plausible then that the expanding shell, previously argued to be due to stellar winds from Wolf-Rayet stars, instead traces a shock front of our SNR candidate. The dense environment, the velocity-based energy estimate ($2 \times 10^{48}$ erg) and is less than the limit derived by the thermal X-ray model and if the velocity-based energy estimate is a lower limit, then the two may be reconciled.

## 8.2 Introduction

The Sagittarius B (Sgr B) cloud, is one of the largest and most complex star forming regions in the Galaxy. Assuming a distance to the Galactic center of 8.5 kpc, Sgr B lies at a projected distance of ~100 pc from the Galactic center and consists of the massive star forming regions Sgr B1 and B2. Both Sgr B1 and B2 have been well studied at all wavelengths, including centimeter radio continuum. Sgr B1 possesses many more large, diffuse HII regions than Sgr B2 does and a different structure of H$\alpha$ lines – signs of relatively more advanced star formation. Sgr B1 appears to be older than Sgr B2 (Mehringer et al, 1995). In contrast, Sgr B2 has many (upwards of 60; Gaume & Claussen (1990), Mehringer, et al. (1993)) ultra-compact HII (UCHII) regions, signs of ongoing massive star formation.

Given that there is so much star-formation within Sgr B2, it would not be surprising if supernova remnants were embedded within the cloud (Lang, Palmer & Goss, 2008). Since the discovery of the Sgr B GMC (Cooper & Price, 1964), there have been many claims of non-thermal emission from the Sgr B2 cloud (see Lang, Palmer & Goss (2008) for a review), however, no convincing argument has ever been made for non-thermal emission from the Sgr B2 molecular cloud itself (this does not include claims of non-thermal emission from larger regions, such as made by Crocker et al. 2007).

Sources which posses a non-thermal spectrum, whether discovered at radio wavelengths or not, are important as a possible probe of the underlying cosmic-ray spectrum. Aharonian et al (2006) discovered extended $\gamma$-ray emission at TeV energies over a large region of the Galactic centre region, which correlates well with the molecular matter – indeed one of the brightest parts of this emission is coincident with the Sgr B cloud. It is noted in Aharonian et al (2006) that whilst a nucleonic interpretation (i.e. that the $\gamma$-rays are created by nucleonic interactions with the ambient molecular matter, leading to the correlation with the molecular line emission) is most likely, a population of electron accelerators cannot be ruled out. Thus, especially in regions of high molecular density, discovery of non-thermal emission from sources which may accelerate particles to TeV energies, such as supernova remnants (SNRs), are important as a means of interpreting the $\gamma$-ray emission in the region as a proxy for the cosmic-ray spectrum.

The source which is the topic of this paper is a source to the south of the Sgr B2 Complex, which hereafter is referred to as the Southern Complex (SC), has previously been noted as a possible non-thermal source (Gray, 1994a; Lang, Palmer & Goss, 2008; Akabane et al., 1988)) in the 843 MHz Galactic plane survey with the Molongolo Observatory Synthesis Telescope (MOST). We have recently observed the entire Sgr B complex at 1384 and 2368 MHz with the Australia Telescope Compact Array (ATCA)[1] Jones et al (2008a) (hereafter referred to as Paper I,) and found that Sgr B2(SC) has a non-thermal spectrum between these frequencies, although the 330 MHz flux listed in LaRosa et al. (2000) hints at the source being absorbed at low frequencies.

This paper describes the analysis of archival radio data and X-ray data on this source, which we suggest is a SNR candidate. Section 8.3 describes the archival radio and X-ray data which we have assembled. In Section 8.4, we present the results of the radio continuum, 1720 MHz OH maser line and X-ray data. In Section 8.5, we discuss interpretations of the data and present our conclusions in Section 8.6.

[1]The Australia Telescope Compact Array are part of the Australia Telescope which is funded by the Commonwealth of Australia for operation as a National Facility managed by CSIRO.

## 8.3 New and Archival Radio & X-ray Observations

In this section, we briefly summarise the radio line and continuum data which are summarised in Table 8.1.

### 8.3.1 Archival ATCA Radio Continuum Data

#### 1384 and 2368 MHz ATCA data

At 1384 and 2368 MHz ($\lambda$20/13 cm respectively), we used the single pointing 1.5C array configuration data *only*, as described in Section 6.3 of Paper I. This is so that any differences in data collection is minimized, since both data sets were collected concomittantly as a mosaic of a larger region. The images have a resolution of $47'' \times 14''$ and $27'' \times 8''$ at 1384 and 2368 MHz respectively. The RMS sensitivity in these images is 10 mJy beam$^{-1}$ at 1384 MHz and 5 mJy beam$^{-1}$ at 2368 MHz. Figure 8.1 shows the 1384 MHz image of Sgr B from Paper I, in which Sgr B2(SC) is labelled.

#### 4800 MHz ATCA data

In order to derive a flux density at a higher frequency which is sensitive to the same size scales as the original data, we have obtained archival ATCA data (Project code C064; P.I. J. Whiteoak[2]). Serendipitously, the archival data contains observations conducted with the 1.5A and the EW375 configurations of the ATCA. The 1.5A configuration, at 4800 MHz gives complementary *uv*-coverage to the VLA 4800 MHz observations, whilst the EW375 configuration data gives complimentary *uv*-coverage to the 1.5C configuration ATCA data described in Paper I.

The 1.5A array-configuration utilizes five of a possible six antennae and covering baselines on an east-west track from 153 m to 1.4 km, whilst the EW375 array configuration (also utilizing five antennae) covers baselines on an east-west track from 31 m to 459 m. Observations for both configurations were conducted at 4800 MHz ($\lambda$6 cm), spanning 128 MHz in bandwidth and recording all four polarization products. At 4800 MHz, the FWHM primary beam (FoV) of the ATCA is $9'.9$.

For the 1.5A array configuration data, the total integration time was 446 minutes. Flux density calibrations were undertaken with PKS 1934-638 (3C84) while phase calibrations were undertaken with PKS 1921-293 and PKS 1730-130 from the ATCA calibrator catalog. The resulting images have a resolution of $16''.5 \times 8''$ with an RMS sensitivity of 4 mJy beam$^{-1}$ .

For the EW375 configuration data, the total integration time was 555 minutes. Flux density calibrations were undertaken using the same flux and phase calibrators as for the 1.5A array data. The resulting images have a resolution of $44'' \times 21''$ and an RMS sensitivity of 10 mJy beam$^{-1}$ .

#### 1720 MHz ATCA Continuum and OH-maser line data

We have obtained 1720 MHz ($\lambda$18 cm) ATCA data from 6C array-configuration observations which utilize all six antennae and covering baselines on an east-west track from 153 m to 6 km. At 1720 MHz the FWHM primary beam (FoV) of the ATCA is $27'.7$. The total integration time was 446 minutes with flux density calibrations undertaken with PKS 1934-638 (3C84)

[2]available at `http://atoa.atnf.csiro.au/`

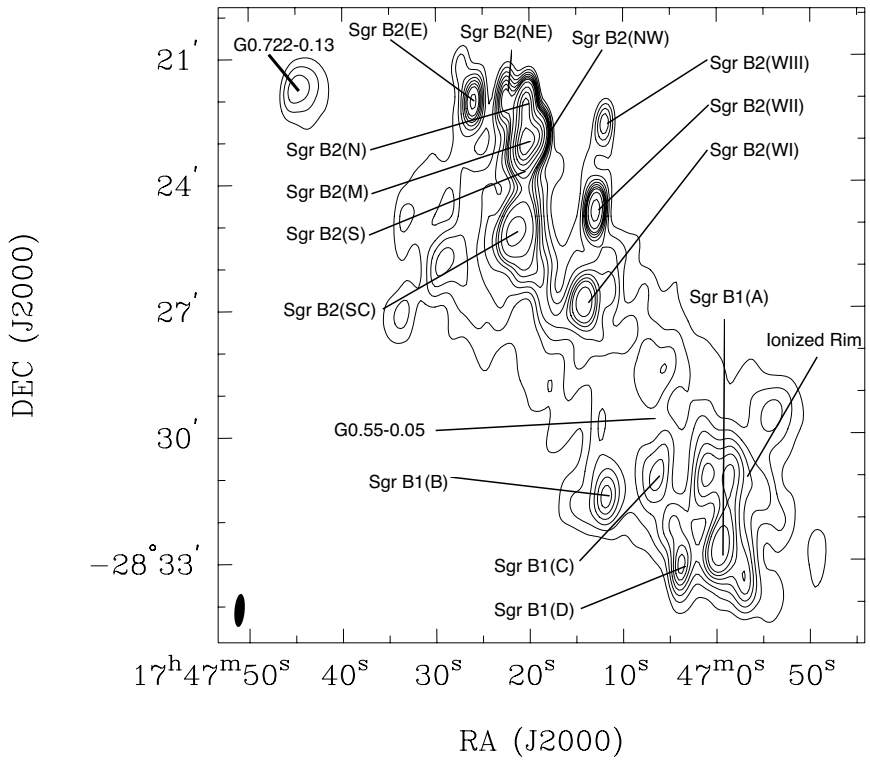


Figure 8.1: Image of 1384 MHz total intensity contours of the Sgr B region from Paper I showing Sgr B2(SC) and other sources. Contours are at 200, 250, 300, 350, 400, 450, 500, 600, 800, 1000, and 1600 mJy beam$^{-1}$ . The image has a resolution of $47'' \times 14''$, which is illustrated by the beam in the lower left-hand corner.

and and phase calibrations were undertaken with PKS 1730-130 and PKS 1921-293 from the ATCA calibrator catalog.

The data was taken in spectral line mode with 4 MHz bandwidth and 2048 channels, and was calibrated and reduced using standard MIRIAD calibration procedures. Line-free channels were used to subtract the continuum emission from all channels to form spectral-line data cube and continuum image. The final image resolution is $11'' \times 4''$ (P.A. = 18.6 degrees).

| $\nu$ (MHz) | Telescope | Beam size($''$) | RMS (mJy bm$^{-1}$) | Ref. |
|---|---|---|---|---|
| (1) | (2) | (3) | (4) | (5) |
| 330 | VLA | $43 \times 24$ | 5 | LaRosa, et al.l (2002) |
| 1384 | ATCA | $47 \times 18$ | 10 | Paper I |
| 2368 | ATCA | $30 \times 9$ | 5 | Paper I |
| 4800 | ATCA | $44 \times 21$ | 5 | This work |
| 4800 | VLA | $7 \times 4$ | 1.5 | Mehringer, et al (1992) |
| 4800 | ATCA | $8 \times 16$ | 2 | This work |
| 8640 | VLA | $4 \times 2$ | 1.5 | Mehringer, et al (1992) |

Table 8.1: Observational parameters for the available data.

### Archival 4800 and 8640 MHz VLA data

We have obtained (already deconvolved) archival 4800 and 8640 MHz data from the Astrophysical Data Image Library (ADIL)[3], which was published in Mehringer, et al. (1993).

[3] http://adil.ncsa.uiuc.edu/QueryPage.html

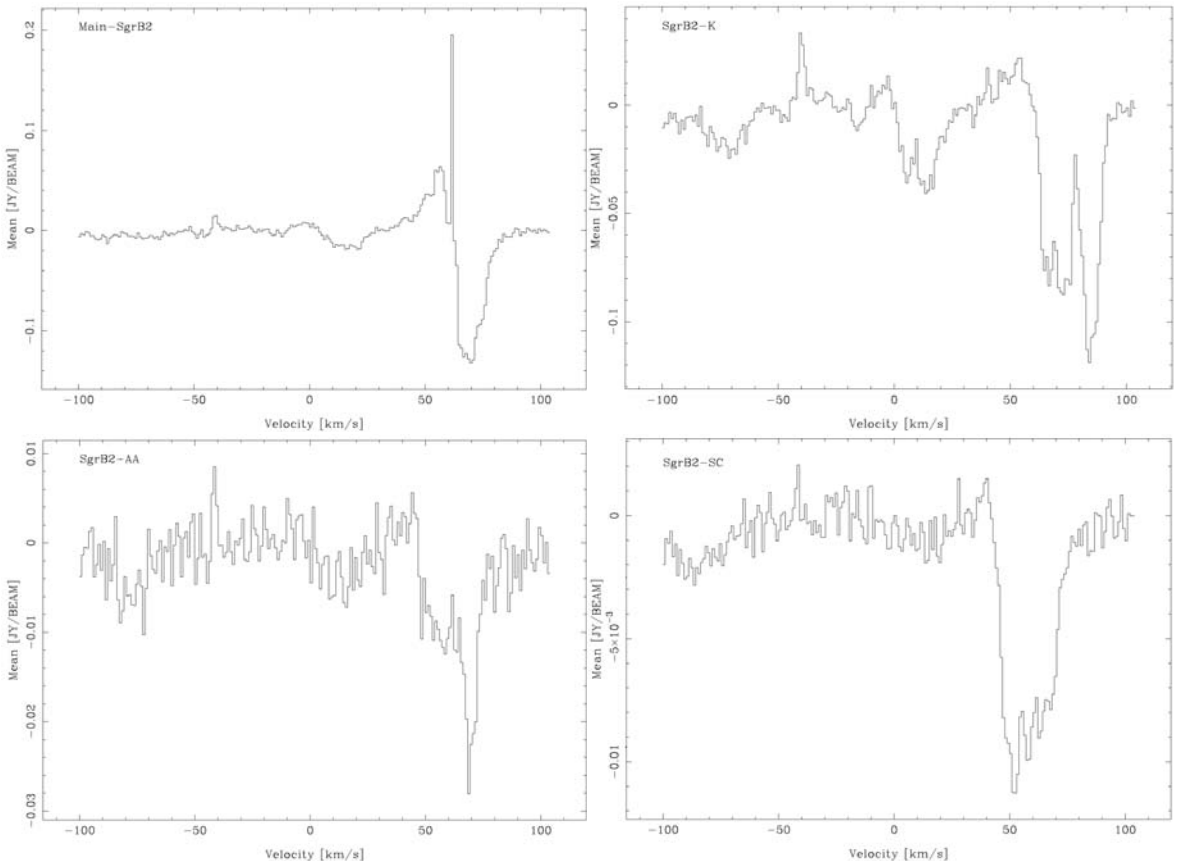


Figure 8.2: Line profiles of 1720 MHz OH absorption for Sgr B2(M) (top, left); Sgr B2(K) HII region (top, right); Sgr B2(AA) HII region (bottom left); and Sgr B2(SC) (bottom, right), showing the features along the line of sight to different components of Sgr B2.

Image resolutions and sensitivities are listed in Table 8.1

### 8.3.2 X-ray data

#### Archival *XMM-Newton* X-ray observations

Sgr B2 was observed with *XMM-Newton Observatory* on 2004 September 4 with a 51 ks exposure. In our analysis we concentrate only on the extended emisison towards Sgr B2(SC) region. The European Photon Imaging Camera (EPIC)-MOS cameras were operated in full window mode with medium filter, while the EPIC-PN camera were operated in full window extended mode with medium filter. The EPIC data reduction was performed using the SAS software package version 8.0.0. The event files used for analysis were created from observational data files (ODFs) using the standard procedure in SAS. The net exposure time after filtering event files for good time intervals was close to the original exposure time. *XMM-Newton* detectors offer spatial resolution between 6″ and 15″.

#### Archival *Chandra* X-ray observations

We also obtained archival *Chandra X-ray Observatory* data of Sgr B2, which was observed with the Advanced CCD Imaging Spectrometer (ACIS) detector on 2000 March 29 with a 100 ks exposure. Again, in our analysis of the *Chandra* data, we examined only the spectral properties of the extended faint emission component that might be related to the Sgr B2 SC source. A detailed analysis of the data is given in Murakami et al. (2001) and Takagi,

Murakami & Koyama (2002). Data were taken in timed exposure mode with an integration time of 3.2 s per frame and accumulated in faint mode. We made use of pipeline processed data, which used the latest software, version DS 7.6.10. *Chandra* detectors offer spatial resolution of better than 1″.

## 8.4 Results

### 8.4.1 Image deconvolution & Flux determination

To produce the images presented in this paper, each set of data was calibrated separately using standard calibration procedures of the MIRIAD software package. Imaging was then performed by Fourier transforming the data using the MIRAD task *invert*, and deconvolved using the MIRIAD task *clean*.

At each frequency for which we posses *uv*-data, the flux density measurement was obtained in the following manner:

1. Each image was produced on a grid of a common scale, and deconvolved using the same Gaussian restoring beam.
2. For every image, the flux density was integrated within the 400 mJy beam$^{-1}$ contour of the 1384 MHz image, shown in Figure 8.1 which corresponds to the level at which the source is separate to the low-level emission surrounding Sgr B2.
3. Because of possible contamination of the flux density due to the low-level background emission, cross-cuts were used to estimate the amount of flux to subtract to establish zero-levels. The average background was then subtracted from the integrated flux (this effect is mainly important at 330 and 1384 MHz).

| $\nu$ (MHz) | Telescope | Res. (″) | $S_\nu$ (Jy) | Ref. |
|---|---|---|---|---|
| (1) | (2) | (3) | (4) | (5) |
| 330 | VLA | $43 \times 24$ | $\sim 0.8 \pm 0.4$ | LaRosa, et al.l (2002) |
| 1384 | ATCA | $47 \times 18$ | $1.2 \pm 0.05$ | Paper I |
| 2368 | ATCA | $30 \times 9$ | $0.8 \pm 0.02$ | Paper I |
| 4800 | ATCA | $44 \times 21$ | $0.6 \pm 0.1$ | This paper |
| 4800 | VLA | $7 \times 4$ | $0.12 \pm 0.001$ | Mehringer, et al. (1993) |
| 4800 | ATCA | $8 \times 16$ | $0.14 \pm 0.01$ | This paper |
| 8640 | VLA | $4 \times 2$ | $0.34 \pm 0.001$ | Mehringer, et al. (1993) |

Table 8.2: Integrated flux density derived by the methods described in the text for Sgr B2(SC).

The archival 4800 and 8640 MHz VLA data, for which we posses final images only, were convolved and re-gridded to match the ATCA images using standard MIRIAD tasks. As such, flux density measurements for these images are more uncertain than those for which we have the raw data. The agreement between the archival ATCA and the 4800 MHz VLA data leads us to conclude that the data is of sufficient quality for measuring the flux densities. Additionally, we have removed from the flux densities listed in Table 8.2, a contribution from the unrelated HII region Sgr B2-AA (Mehringer, et al., 1993) to the northwest of Sgr B2(SC) (c.f. Figure 8.3).

It is important to note that the difference between the flux densities given in Paper I for Sgr B2(SC) and those given here arise from the fact that in Paper I , the mosaic observations

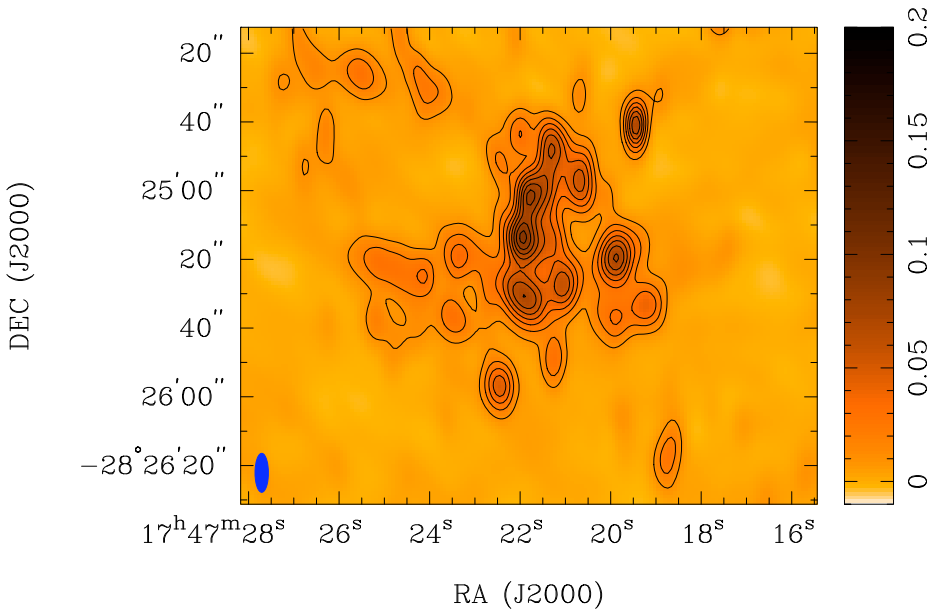


Figure 8.3: Total intensity radio continuum ATCA image at 1720 MHz overlaid with the same (black) contours at: 10, 20, 30, 40, 50, 60, 70, 80 and 90 mJy beam$^{-1}$ (10 mJy beam$^{-1}$ = 5$\sigma$). The resolution of the image is 11″ × 3″ as indicated by the beam located in the lower left-hand corner. The intensity scale (on the right-hand side of the image) is from -10 to 200 mJy beam$^{-1}$ , and a logarithmic transfer function has been applied to the image to emphasise the low-level emission.

(as described there) were used which contains *uv*-data which is sensitive to large scale structures.

Table 8.2 shows the integrated flux density for Sgr B2(SC) using the procedures described above. Columns are (1) the central frequency of the observation; (2) the telescope used; (3) the natural resolution of the observations; (4) the integrated flux density performed on the convolved data set, as described above; and (5) the reference for the description of the data set.

The interferometric nature of the data that we have used at all frequencies means that there should be no contribution from the large-scale Galactic synchrotron background. We have also taken steps to separate the flux density of our source to that of the larger diffuse thermal and non-thermal emission upon which Sgr B2 sits.

### 8.4.2 1720 MHz OH line and continuum emission

The 1720 MHz OH emission and absorption profiles toward a few different regions of Sgr B2 complex are shown in Figure 8.2 in the velocity range −100 to +100 km s$^{-1}$. The spectra have been hanning-smoothed by 3 channels, giving the final spectral resolution of 1 km s$^{-1}$. Prominent features are present around −40 km s$^{-1}$, and between +50 and +90 km s$^{-1}$. The three profiles towards Sgr B2-main (top-left), Sgr B2-AA (bottom-left) and Sgr B2(SC) (bottom-right) show similar strength of these line features. The profile towards the northern part of the Sgr B2 complex, Sgr B2-K (top-right), shows additional features at around −70 km s$^{-1}$and +15 km s$^{-1}$. All these features have been seen in previous OH observations (Whiteoak & Gardner, 1976). The clouds associated with Sgr B2 complex have velocities between +50 and +85 km s$^{-1}$, while the other features originate from absorbing clouds associated with the Galactic spiral arms in the direction of Sgr B2. We have not detected 1720 MHz OH masers towards the SC region, with the 1$\sigma$ rms value of 7 mJy.

Figure 8.3 shows an image of the line-subtracted continuum data at 1720 MHz overlaid with the same (black) 1720 MHz contours. At $11'' \times 4''$ resolution, this represents the highest resolution image available to us, and resolves the same structure as seen at 4.8 GHz in Mehringer, et al. (1993), whose data shows a shell-like object coincident with a similar morphological structure at 1720 MHz. Figure 8.3 also shows a low-level extension of the Sgr B2(SC) source to the east of the source which has not been seen at other wavelengths.

### 8.4.3 X-ray results

Previous X-ray missions (*Ginga* and *ASCA*) have found that Galactic Center region has a large scale diffuse X-ray emission (GCDX) with temperature of ~ 6 keV and prominent lines of 6.4, 6.7 and 6.9 keV Fe (eg Koyama et al. (2007b)). The 6.4-keV Fe line is particularly strong towards Sgr B2 region (Koyama et al, 1996), and it was suggested that represents an X-ray reflection nebula (XRN), irradiated by the strong X-ray source Sgr A* in the centre of Galaxy (eg, Koyama et al (1996), Murakami et al. (2000)). Murakami et al. (2001) investigated diffuse X-ray emission from Sgr B2 with high-resolution *Chandra* observations and determined that this diffuse emission is not simply a contribution from unresolved point sources (which is only 3% of the total flux) or young stellar objects (which have different X-ray spectrum), supporting the XRN scenario. Thus, we are likely to find contributions from one or both of these components (GCDX and Sgr B2) in our spectra.

The exposure-corrected combined EPIC image of Sgr B2 in energy band between 1.5 and 8 keV is shown in Figure 8.4. There is extended emission towards Sgr B2(SC), as shown in Figure 8.5, where X-ray grayscale is overlaid with radio contours. We extract source spectra from a 48″-radius region towards the location of the radio source.

| Parameter | Value |
|---|---|
| $n_H$ ($\times 10^{22}$ cm$^{-2}$) | $12.5^{+2.8}_{-1.0}$ |
| Low-$T$ component | |
| $kT$ (keV) | $0.15^{+0.08}_{-0.03}$ |
| $n_e t$ ($\times 10^{11}$ cm$^{-3}$ s) | $7.2^{+0.4}_{-5.0}$ |
| $EM$ (cm$^{-3}$) | $< 1.2 \times 10^{60}$ |
| High-$T$ component | |
| $kT$ (keV) | $> 10.0$ |
| $n_e t$ ($\times 10^{11}$ cm$^{-3}$ s) | $6.5^{+4.3}_{-2.2}$ |
| $EM$ (cm$^{-3}$) | $3.8^{+0.7}_{-0.8} \times 10^{56}$ |
| Gaussian line component | |
| $E$ (keV) | $6.34^{+0.02}_{-0.02}$ |
| $dE$ (keV) | $\times 10^{-4}$ (frozen) |
| $K$ (photons cm$^{-2}$ s$^{-1}$) | $4.9^{+2.1}_{-2.4} \times 10^{-4}$ |
| $\delta\chi^2$/dof | 1.12/127 |
| Unabsorbed X-ray flux (2.0–10 keV) | |
| $F_{\rm total}$ ( erg s$^{-1}$ cm$^{-2}$) | $9.8 \times 10^{-13}$ |

Table 8.3: Results from fitting VPSHOCK+VPSHOCK+GAUSS model with the 90% confidence ranges.

The background spectra were extracted from a same-radius low-emission region towards the edge of the field. This background region will contain a contribution from the cosmic X-ray background and non-X-ray (instrumental) background, as well as from GCDX and Sgr B2 diffuse emission. We subtract this background spectra from the source spectra, and

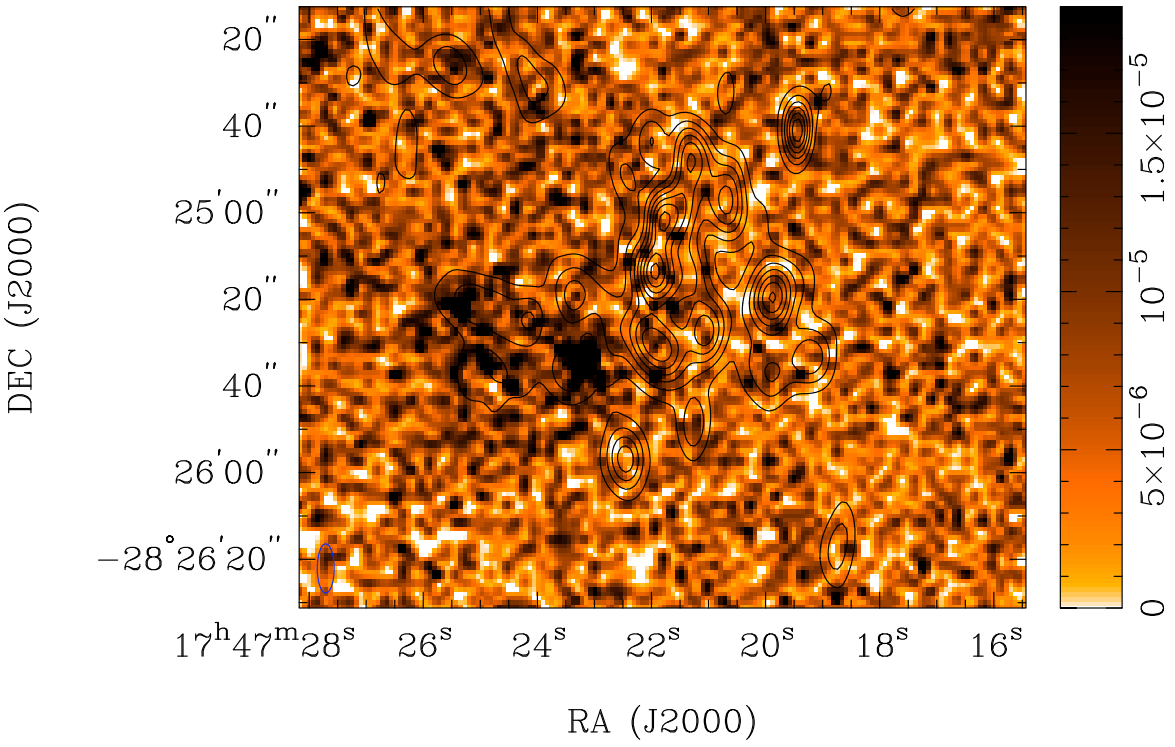


Figure 8.4: Exposure corrected count map of the 50 ks XMM-Newton observations overlaid with 1720 MHz (black) contours (same levels as in Figure 8.3).

fit the three spectra from the each EPIC detector simultaneously. The source spectra yield ~ 700 total or ~ 400 background-subtracted counts from each detector. The spectra are shown in Figure 8.6. Emission lines from 1.8-keV Si line and 6.4 and 6.7 keV Fe lines are clearly visible in the spectra, indicating that there is a residual component of the GCDX emission (Fe lines) and that there is most likely contribution from another thermal plasma (Si line). We first fitted the data with a single thermal plasma model, which gave column density of $1.5 \times 10^{23}$ cm$^{-2}$, plasma tempearture of ~ 8 keV and reduced $\chi^2$ of ~ 1.7. The high $\chi^2$ was mainly because the Si and Fe lines were not well fitted.

We then added a second component to the fit, using either a thermal plasma model or a power law model. Adding the second thermal component did improve the fit significantly ($\chi^2$ went from 219 for 136 d.o.f. to 170 for 131 d.o.f. for VPSHOCK model, see below), while adding the power law component did not improve the fit.

A plane-parallel shock model with ionizing plasma (VPSHOCK; Borkowski et al. 2001) was preferred in the spectral fit over a model of thermal plasma in ionization equilibrium (VRAY; Raymond et al. 1977), although the values of the fit parameters do not differ much. Both type of fits are significantly improved when a gaussian component was added to account for the strong 6.4 keV line ($\chi^2$ went from 170 for 131 d.o.f. to 141 for 127 d.o.f. for VPSHOCK model). The fit parameters are shown in Table 8.3. The absorbing column density $N_{\rm H} \sim 1.25 \times 10^{23}$ cm$^{-2}$ is similar to what was found towards Sgr B2 point sources (Takagi, Murakami & Koyama, 2002). The first thermal component with plasma temperature $kT \sim 10$ keV and the presence of strong 6.4 keV line corresponds to extended GCDX/Sgr B2 emission, implying that we have not subtracted this component completely, as expected. The plasma temperature of the second component of $kT = 0.15$ keV could then be associated with our radio SNR candidate, Sgr B2(SC). We also extracted source spectra from two smaller regions: one that coincides just with the bright radio western emission, and the other that

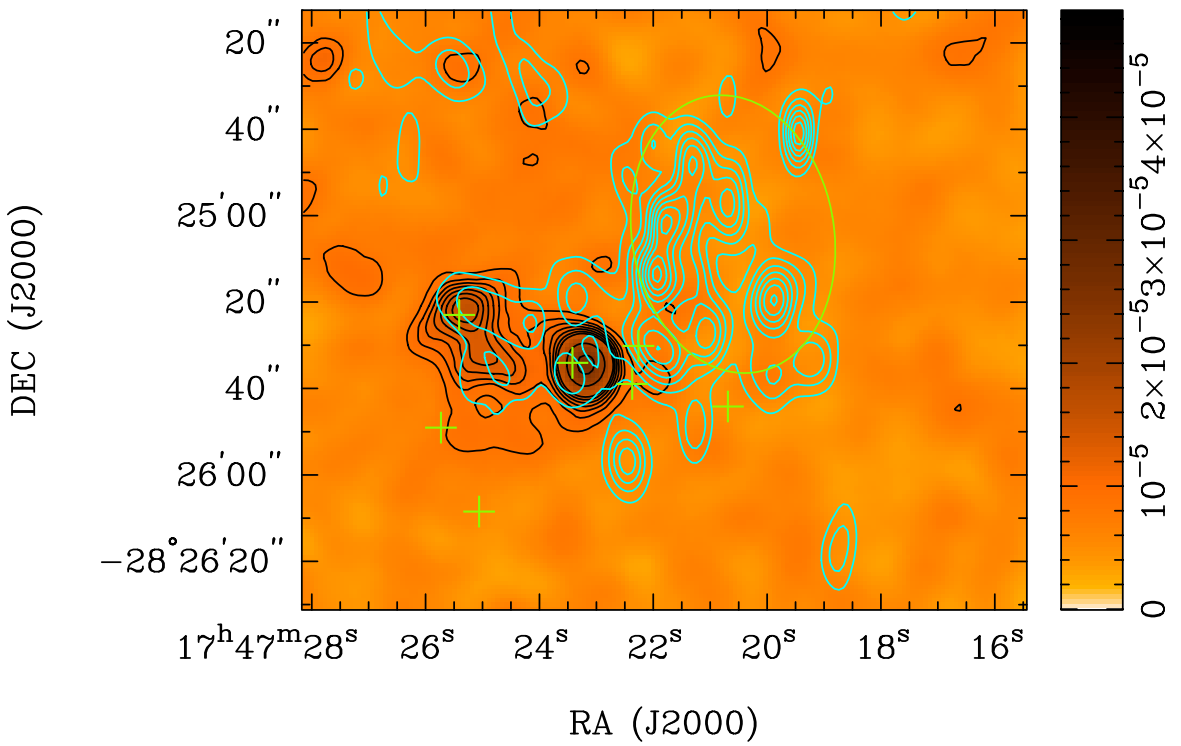


Figure 8.5: Gaussian smoothed XMM-Newton image of Sgr B2(SC) overlaid with (aqua) X-ray contours and (black) 1720 MHz ATCA contours at levels the same as in Figure 8.3. The X-ray contours are at: 0.85, 1.0, 1.1, 1.2, 1.3, 1.4, 1.5, 2.0, $2.5\times10^{-5}$ erg s$^{-1}$ cm$^{-2}$. The crosses are the positions of the X-ray point sources from *Chandra* observations Muno et al. (2006). The ellipse is the approximate position and size of Shell F from Martin-Pintado et al (1999)

coincides just with the brightest X-ray emission. In both latter cases, we get about 150-200 background subtracted counts, which does not provide enough statistics to constrain any model.

Thus we derive values of the SNR parameters using the spectral parameters of the second thermal component. The post-shock temperature for the Sedov phase is $kT_s \approx 0.77kT_X \sim 0.11$ keV, and the corresponding blast wave velocity is $v_s = (16kT_s/3\mu m_{\rm H})^{1/2} \sim 314$ km s$^{-1}$, where $\mu$ is the mean atomic weight.

To derive plasma parameters for the two plasma components, we denote $f_l$ and $f_h$ as filling factors for the low and high temperature components, and assume that the two components are roughly in pressure equilibrium. We derive relative filling factors: $f_h/f_l = (EM_h/EM_l)/(T_l/T_h)^2$ (e.g. Lazendic et al. 2005). We find that $f_h/f_l < 1.3f$, where $f$ is the unknown volume filling factor from which X-ray emission is emitted. The electron densities are then $n_l \gtrsim 77.5\ f^{-1/2}d^{-1/2}$ cm$^{-3}$ and $n_h \gtrsim 1.2\ f^{-1/2}d^{-1/2}$ cm$^{-3}$, where $d$ is the distance to the source. The X-ray emitting mass is $M_l \lesssim 118\ fM_\odot$ in the low temperature component and $M_h \leq 0.5\ fM_\odot$ in the high temperature component. The SNR explosion energy is then $E_l \gtrsim 4.1\times10^{49}$ erg. The age of the remnant is found to be $t = 2r_s/5v_s \sim 3000$ yrs, where $r_s$ is the radius of the source and $v_s$ is the velocity of the shock.

We examined archival *Chandra* observations to search for extended emission towards Sgr B2(SC) region, but find no obvious emission feature. We found only about 30 counts in the region corresponding to the radio source Sgr B2(SC), which was insufficient for spectral fitting.

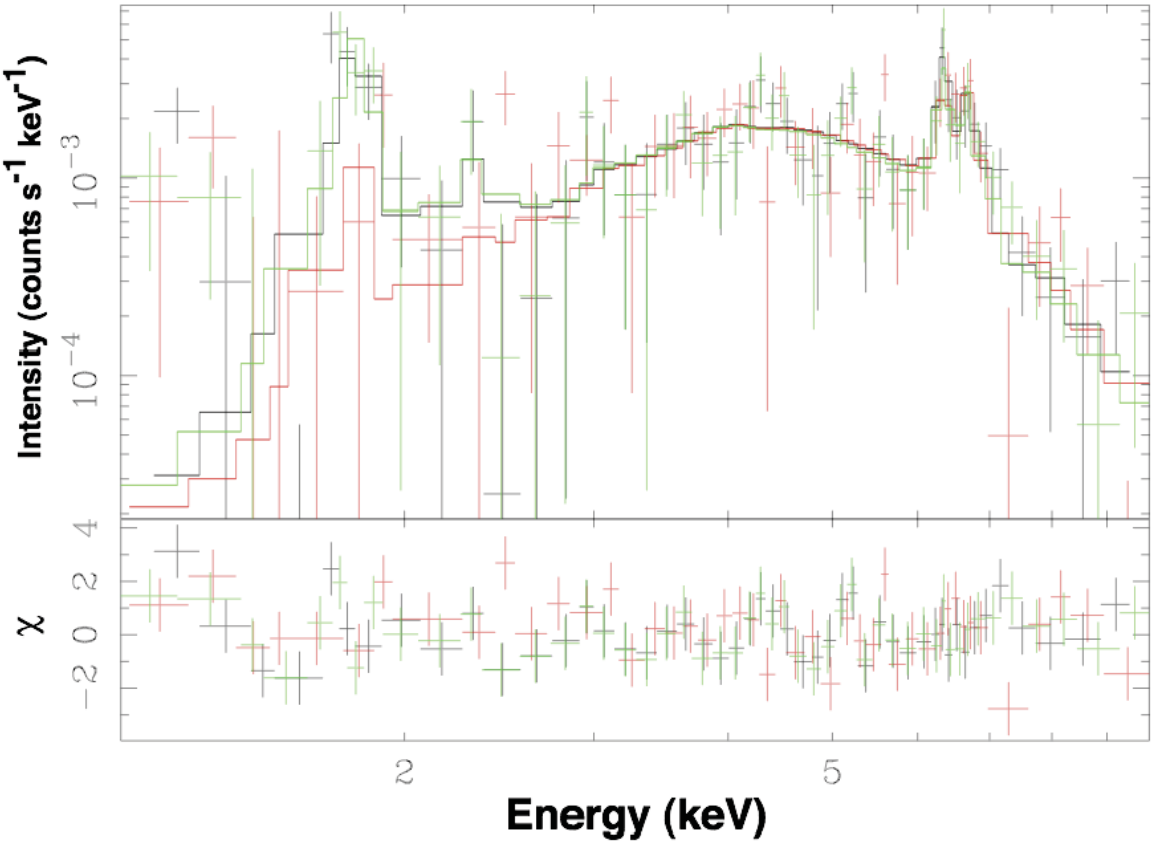


Figure 8.6: X-ray spectrum of Sgr B2(SC) extracted from the *XMM-Newton* data as described in the text.

## 8.5 Discussion

### 8.5.1 Radio and X-ray Morphology

Inspection of Figure 3 of Paper I shows that the non-thermal emission from the region at 1.4 and 2.4 GHz is coincident with a shell of radio emission to the southeast of Source AA described in Mehringer, et al. (1993) and is the source which has been described as possibly non-thermal in past studies of Sgr B2. The higher resolution (than the 1.4 and 2.4 GHz images presented in Paper I ) image shown in Figure 8.3 shows that the radio continuum emission at low frequencies follows that of the higher frequency data (i.e., the 4800 and 8640 MHz VLA images).

Figure 8.5 shows an image and (black) contours of the Gaussian smoothed *XMM-Newton* data overlaid with (aqua) contours of the 1720 MHz line-subtracted continuum data. This figure illustrates the correspondence between the easterly extension of the 1720 MHz data and the X-ray source: peaks in the X-ray intensity correspond to the peaks in the radio continuum intensity. There is no correspondence, on the other hand, of the X-ray emission with the radio continuum to the north-west, which in the radio continuum is dominated at all frequencies by shell like emission. This is not surprising, however, given the high column density towards Sgr B2 and GC region, which makes this region opaque for 2 – 8 keV X-ray photons.

The line-subtracted 1720 MHz continuum emission shown here is – so far – the only frequency at which this emission is observed. On the basis of the intensity of this emission, we find that even in spite of the absorption (as described below) observed in the lower

resolution 330 MHz images, such an extension would lead to a marginal $2\sigma$ detection at 330 MHz using higher resolution 330 MHz images of Nord et al (2004). Inspection of this data reveals no significant extension to the (already) weak SC source.

#### Synchrotron Self-absorption

Although the radio continuum spectrum at low-frequencies could be due to synchrotron self-absorption (SSA), we argue that this is not the case, since SSA usually occurs in very compact regions, such as the cores of the jets of active galactic nuclei. A simple physical argument can be used to show that the low-frequency turnover that Sgr B2(SC) exhibits is not due to SSA. For non-thermal sources exhibiting SSA, the emission is optically thick when the brightness temperature exceeds the effective temperature of the electrons which are emitting the (presumably) synchrotron photons. In the case of Sgr B2(SC) with a magnetic field value of $\sim 1$ mG and a linear size of $\sim 1.25$ pc, the effective temperature of the electrons at 1 GHz is $T_{eff} \sim E/k \sim 10^{12}$ K, whereas the brightness temperature is $T_b \sim 1000$ K for an intensity of $\sim 1$ Jy. Thus SSA is unlikely to be the reason for the spectral downturn between 1.4 GHz and 330 MHz.

#### Synchrotron emission in high density regions & possible role of secondary electrons

Table 8.2 shows that Sgr B2(SC) exhibits a non-thermal spectrum which matches that expected from synchrotron emission due to a power-law distribution of relativistic electrons. It was shown in Paper I that the non-thermal emission from this region is not due to secondary electrons because the high densities found in the region (c.f. Figure 5 of Paper I) work to limit the emissivity of any secondaries created.

However, at low frequencies bremsstrahlung losses will begin to dominate synchrotron losses in regions of high density because of the kinematics of the charged pion production. In this scenario, a flattening and eventual turnover (from a negative spectral index to a positive one) at low frequencies can occur. Given that the $NH_3$ observations indicate that the ambient molecular density in the region is $\sim 10^3$ cm$^{-3}$ , we have attempted to fit the spectrum using parameters which produce such a turnover. We find, however, that the turnover produced is too flat and too gradual to reproduce the observed spectrum. Thus we conclude that the spectrum presented in Table 8.2 is due to primarily accelerated electrons.

#### Properties of the CR spectrum and constraints on the X-ray source modelling

A spectral index of $\alpha = -0.8$ for the synchrotron photons implies that between 1384 and 2368 MHz the observed emission originated from a parent electron spectrum of index $\gamma = 2\alpha + 1 = 2.46$ for a power-law distribution of electrons (i.e., $dN/dE \propto E^{-\gamma}$). The flatter spectral index of the emission at higher frequencies can be explained by the presence of the thermal source Sgr B2(AA) nearby if the conditions produce a source which is optically thick at frequencies $\gtrsim 2368$ MHz (since an optically thin source would work to flatten the lower frequency flux densities as well).

At lower frequencies, the implied electron spectral index is steeper than the usual particle spectrum derived from calculations of particle acceleration in SNR shocks (i.e. diffusive shock acceleration). However, given that the X-ray derived, best-fit age for our SNR candidate is $t \sim 3000$ years, a steeper spectrum could be due to the energy dependent electron cooling and confinement time. This occurs when the SNR is old enough so that a

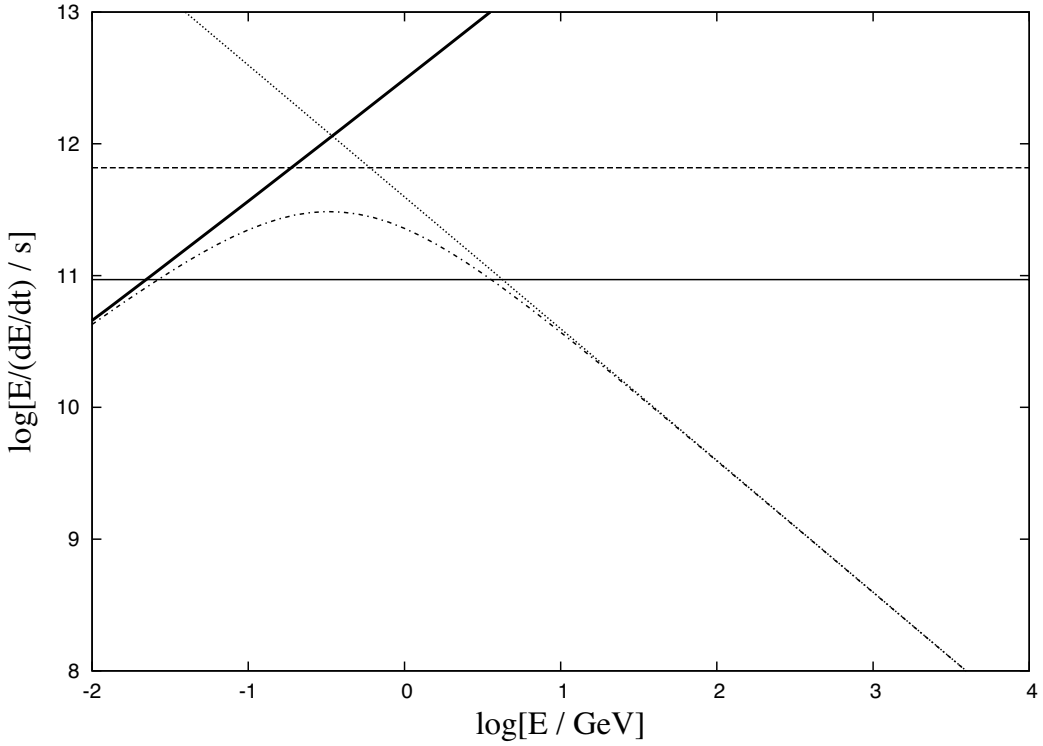


Figure 8.7: Loss-times for various loss processes in a region of ambient molecular density of $\sim 10^3$ cm$^{-3}$ (estimated using Figure 2 of Protheroe et al. 2008) and a magnetic field of 1 mG. The loss processes shown here are: ionization (thick black line); bremsstrahlung (dashed line); synchrotron (dottes line); and the total (sum) loss-times (dot-dashed line). Also shown as the thin (solid) line is the age of the SNR as per the best-fit X-ray model in Table 8.3.

significant proportion of the particles accelerated in the remnant have either: (i) diffused away, or (ii) lost a significant fraction of their original energy. In both cases, the result is a spectrum which, as the SNR ages, becomes steeper at lower frequencies.

Possessing an estimate of the magnetic field and ambient hydrogen number density, we have computed the loss times – defined as $E/(dE/dt)$, where $dE/dt$ is the loss rate for the appropriate loss mechanism – to explore whether particle losses can account for the steeper than usual spectral index between 1384 and 2368 MHz. Figure 8.7 shows that, for magnetic field amplitude of 1 mG and an ambient hydrogen number density of $10^3$ cm$^{-3}$ we find that the estimated age of our SNR candidate has provided sufficient time for accelerated electrons to cool and steepen the synchrotron photon spectral index.

### 8.5.2 X-ray emission

The soft plasma component in our *XMM* spectra is well fitted by the absorbed thermal spectrum expected in the Sedov phase of SNR evolution. The SNR parameters derived from the spectral fit imply a middle-aged SNR evolving in dense environment, as found for other SNRs evolving in or near dense molecular clouds (eg, Lazendic et al. 2005). *Suzaku* has reported a detection of an SNR candidate in the Sgr B2 region, G0.61+0.01 (Koyama et al., 2007), which is located in the north-east region of Sgr B2 complex, towards Sgr B1 complex.

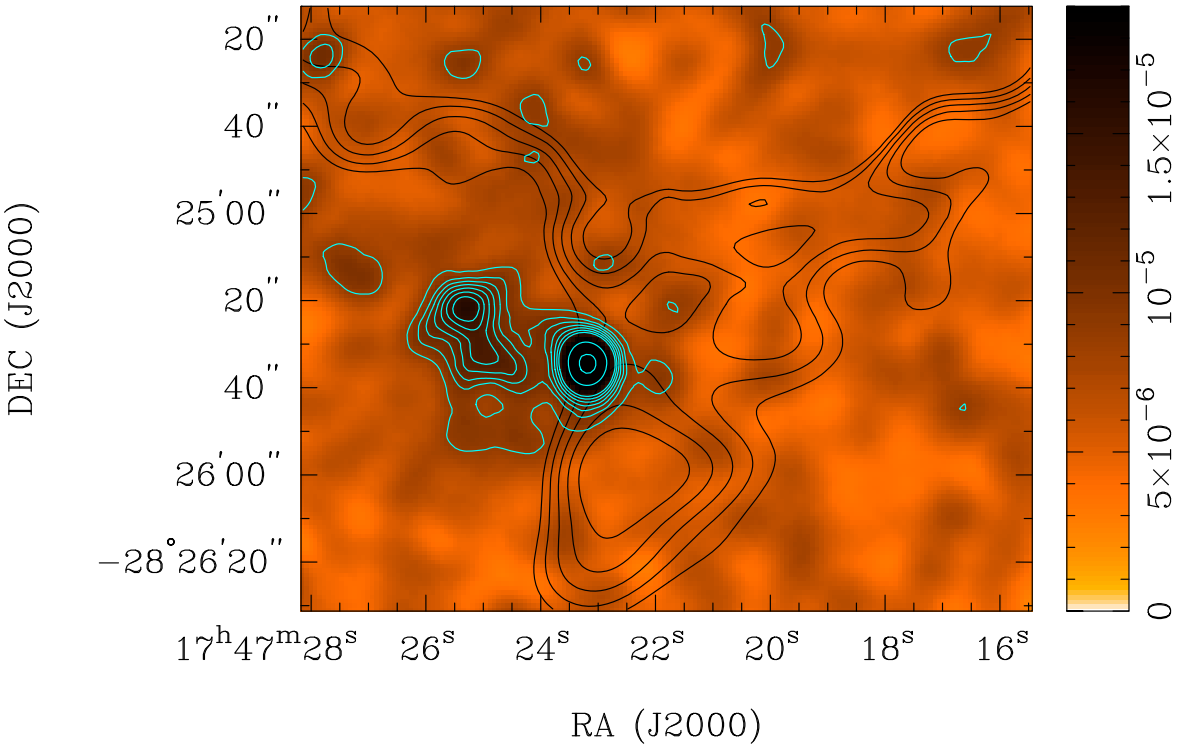


Figure 8.8: Gaussian smoothed X-ray intensity map overlaid with the same (aqua) contours as in Figure 8.5 and (black) peak intensity $NH_3$ contours at 4, 4.5, 5, 5.5, and 6 K.

This SNR has been identified from an excess of 6.7 keV Fe emission in the *Suzaku* data of Sgr B2 region, and was found in archival *XMM Netwon* observations in 6.7-keV image, but not in 2–8 keV continuum image, and could not be confirmed in archival *Chandra* images (Koyama et al., 2007). The *Suzaku* SNR candidate has plasma temperature of ~ 3 keV and overabundance of Fe, similar to another GC SNR Sgr A East (eg. Sakano et al. 2004). A very high absorbing column density of $1.6 \times 10^{23}$ cm$^{-3}$ places this SNR behind or on the rim of Sgr B2 cloud (Koyama et al., 2007). Law et al (2007) report possible non-thermal emission from this region between Sgr B1 and Sgr B2 from the low-resolution radio observations with the Green Bank Telescope.

There are a number of X-ray point sources detected towards Sgr B2 region (Takagi, Murakami & Koyama, 2002), of which several are located in the region of Sgr B2(SC) (Muno et al., 2006) and are shown as (yellow) crosses in Figure 8.5 with two of these point sources are located at maxima in the *XMM-Newton* and 1720 MHz radio continuum data.

Takagi, Murakami & Koyama (2002) found 17 point sources within 1′.5 around the Sgr B2 Main in the pointed *Chandra* observations we consider here. They separate these sources in two categories: type A that can be associated with known HII region, and type B that does not seem to be associated with known HII region. For the first group derived column density is as high as $5{\times}10^{23}$ cm$^{-2}$, and plasma temperature is also high, above 5 keV. The authors suggest that these type of sources are deeply embedded young stellar objects with various mass ranges. Type B sources also have high column density of $1{\times}10^{23}$ cm$^{-2}$, and high plasma temperature above 4 keV, and are suggested to be isolated white dwarfs powered by Bondi-Hoyle accreation. Muno et al. (2006) used, in addition to pointed observations, short (~ 25 ks) Galactic Center survey observations, and derive a catalogue of point sources within 150 pc from GC. There are 5 *Chandra* point sources within 48″ radius towards Sgr B2(SC) with 10 to 70 counts, which converts to about 120 counts in total for *XMM* detectors. That

constitutes about 1/6 of counts extracted from our *XMM* source regions, and this joint point source contribution might be a small part of the hard plasma component which we assigned mostly to GCDX/Sgr B2 extended emission.

*XMM-Newton* data used here have been analyzed by Inui et al. (2008), in combination with *Suzaku, ASCA and Chandra* data. A bright emission region is apparent at the Sgr B2(SC) location in their Figure 1, but it was included as a part of the whole Sgr B2 cloud (source M 0.66–0.02), and the authors were mainly interested in exploring the variability of 6.4-keV line emission.

### 8.5.3 Molecular material and interactions with the SNR candidate

We found no 1720 MHz OH maser emission towards the SC region in Sgr B2, which have been used as tracers of SNR/molecular cloud interaction (Green et al., 1997). This non-detection does not exclude the possibility that SC is a SNR, because to produce this transition of OH masers alone, without accompanying 1665, 1667 and 1612 MHz OH masers, requires a very specific conditions: a gas with temperatures between 50–125 K, density of $\sim 10^5$ cm$^{-3}$ and OH column density of $10^{15} - 10^{17}$ cm$^{-2}$ (Lockett et al., 1999). Such conditions match those of cooling gas behind a non-dissociative C shock, irradiated by the X-ray flux from the SNR interior (Wardle, 1999). The region towards Sgr B2(SC) shows properties of typical Galactic centre molecular clouds – judging from HNCO/$^{13}$CS abundance ratios (Martin et al., 2008) – which implies densities of around $10^4$ cm$^{-3}$ and kinetic temperatures more than 80 K (HNCO and $^{13}$CS are good tracers of dense gas expected in GC region, and are unaffected by opacity effects). Thus the density around Sgr B2(SC) could be (i) lower than needed to produce OH masers; or (ii) the OH column density might be too high because of the additional irradiation by the HII regions. Indeed, the main OH maser lines, that require higher OH column density, have been observed in the region just NW from the SC region (Martin-Pintado et al, 1999).

#### Expanding $NH_3$ shells

$NH_3$ observations have shown that there are numerous hot expanding shells in Sgr B2 region (Martin-Pintado et al, 1999). One of the shells have been found to coincide with the weak radio continuum source next to Sgr B2(AA) from Mehringer, et al. (1993), which is our Sgr B2(SC) source. The $NH_3$ shell (denoted with F) is elliptical in shape and is expanding at velocity of $\sim$ 7km s$^{-1}$. Martin-Pintado et al (1999) suggest that this $NH_3$ shell could be produced by expanding SNR, but is most likely produced by winds from W-R stars, because the kinetic energy associated with this and other shells ($\sim 2 \times 10^{48}$ ergs) is 3 orders of magnitude smaller than those associated with SNRs.

In Section 8.4.3 above, we derived a lower limit to the energy of a possible SNR associated with the X-ray source of $E_l \gtrsim 4.1 \times 10^{49}$ erg, which is about an order-of-magnitude greater than that attributable to WR-stars. The morphology of the $NH_3$ shells is such that it does not cover the entire radio+X-ray source. The parts of the shell which are coincident with our X-ray/radio continuum source are that where the associated density is the greatest (c.f. Figure 8.8), thus it would seem plausible that the mean velocity from which the estimate of the energy is obtained could be a lower limit – as indeed is our estimate from the X-ray data. Given that the column density is so great, the X-ray source must be located on the near side of the Sgr B2 cloud, and that the X-ray emission toward the bright radio emission could be absorbed.

## 8.6 Conclusions

We conclude then, on the basis of the observational and theoretical bases summarized below that we have discovered a previously unknown SNR located on the edge of the Sgr B2 cloud. The lines of evidence upon which we base our conclusions can be summarized as follows:

1. Radio continuum observations with the ATCA which sample consistent parts of the *uv*-plane (of which the 1.4 and 2.4 GHz observations were taken simultaneously) derive a non-thermal spectrum with a spectral index of $\alpha \sim -0.7$ between 1.4 and 2.4 GHz and $\alpha \sim -0.5$ between 2.4, 4.8 and 8.6 GHz. This source has previously been noted as a possible non-thermal source in Gray (1994a). The 330 MHz VLA datum is undervalued, which we argue is due to the synchrotron spectrum becoming optically thick at frequencies below $\sim 1$ GHz.

2. Several molecular and radio recombination lines place the radio continuum emission at a velocity range which is consistent with this source being located at Sgr B2. Additional $NH_3$ observations place the density in the region at $\sim 10^3$ cm$^{-3}$ , which we argue makes the synchrotron emission from this source likely due to primarily accelerated electrons.

3. We have used archival X-ray data from *XMM-Newton* to uncover an extended X-ray source. This source has several features common to Galactic SNRs, such as the presence of a 6.7 keV Fe line, and a 1.8 keV Si line. Additionally, spectral fitting of the X-ray data shows that this source has two components – an 8 keV component consistent with the background Sgr B2 emission – and an additional 0.15 keV component for which the spectral fitting of a SNR shock model produces features which are common to SNRs near the Galactic centre.

4. High resolution (relative to the 1.4 GHz ATCA data) 1720 MHz ATCA data reveals a low-level radio continuum feature which morphologically matches the extended X-ray emission. $NH_3$ molecular line observations show that there is a high density gradient from the peak in the radio continuum source towards the X-ray source.

5. Higher resolution $NH_3$ observations with the VLA have revealed $NH_3$ shells (Martin-Pintado et al, 1999), one of which is partially coincident with our radio and X-ray data. We argue that the high density in the region is retarding the expansion of these shells, and the implied energy in the shells is a lower limit.

# 9 The Large Scale Magnetic Field Intensity of the Galactic Center Region

## 9.1 Introduction

This chapter is based on a paper which has been submitted to Nature (Crocker et al., 2008), where we set out the arguments which illustrates the two orders-of-magnitude uncertainty of the amplitude of the large-scale magnetic field permeating the Galactic centre region and show that at the very least, one can reduce this uncertainty by an order-of-magnitude. We argue that there is a lower limit to the large-scale magnetic field amplitude of 100 $\mu$G and outline evidence that the actual value is near this lower limit of 100 $\mu$G.

In this chapter, we define the DNS as a region of the GC region which covers an elliptical region of 3° semi-major axis (along the Galactic plane) and 1° semi-minor axis, centered on the dynamical centre of the Galaxy. This corresponds to a physical radius of $\sim$ 420 pc and half-height of $\sim$ 140 pc at the assumed GC distance of 8 kpc (the reason for such a definition is to be consistent with LaRosa et al 2005).

## 9.2 Existing evidence for the large-scale magnetic field amplitude

For the last twenty-five-or-so years, the exact amplitude of the large-scale magnetic field pervading the GC region has been uncertain by at least two orders-of-magnitude. This is because two separate lines of evidence have concluded that the amplitude of the field is either 10 $\mu$G or 1 mG. Below we set out the evidence in favour of each case.

### 9.2.1 Evidence for a *weak* large-scale field:

Figure 9.1 shows the diffuse non-thermal radio source (DNS) as revealed by LaRosa et al (2005). Using this image, and similar data at 74 MHz, LaRosa et al (2005) found a flux density of at least 16.2 ± 1 kJy at 74 MHz and 7 kJy at 330 MHz, giving a spectral index (assuming $S_\nu \propto \nu^\alpha$) of at least $\alpha = -0.7$ (the spectral index here is an upper limit, since the 74 MHz flux is a lower limit due to the attenuation of the flux due to HII regions between us and the DNS: an increase in the 74 MHz flux density will decrease the spectral index, i.e., make it more negative. This fact, as LaRosa et al (2005) argued, does not affect their analysis).

Using this spectral index and normalisation, LaRosa et al (2005) integrated the flux density from 10 MHz to 100 GHz to find a synchrotron luminosity of the DNS of $\sim 3 \times 10^{36}$ ergs s$^{-1}$. The luminosity can then be used to estimate the minimum energy density in the magnetic field required to explain the observed radio luminosity by assuming that the magnetic field energy density is in equipartition with the cosmic ray energy density. The

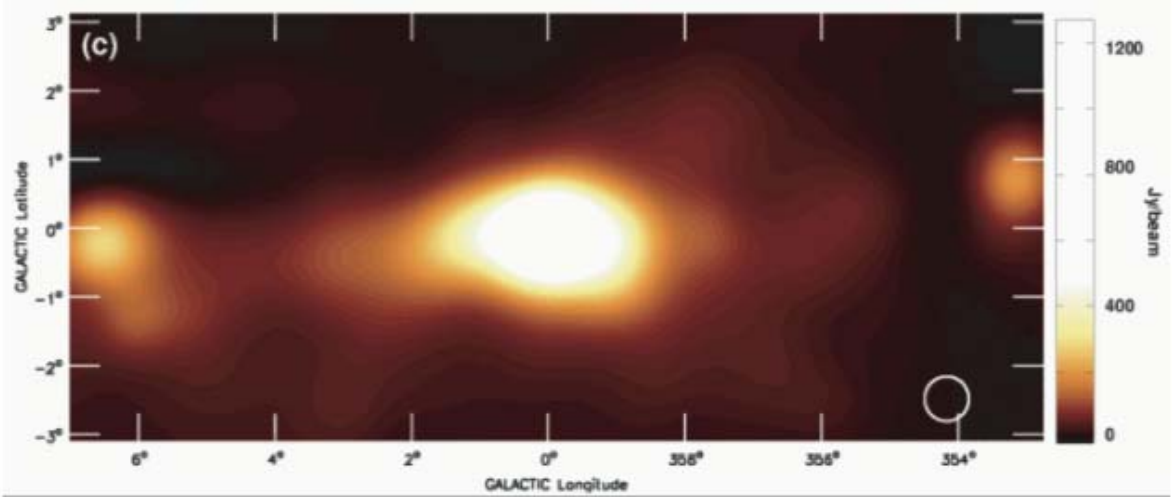


Figure 9.1: The DNS at 330 MHz from LaRosa et al (2005) (Figure 1c) obtained using the GBT and subtracting the Galactic synchrotron background.

minimum cosmic ray energy is then given by Moffat (1975):

$$U_{min} = 0.5(\phi AL)^{4/7} V^{3/7}, \tag{9.1}$$

where $A$ is a function of the spectral index, $L$ is the luminosity (given above), $V$ is the volume of the DNS region and $\phi$ is the volumetric filling factor. This gives an estimate for the magnetic field amplitude of:

$$B(U_{min}) = 2.3(\phi AL/V)^{2/7}. \tag{9.2}$$

Inserting the derived values for each parameter, LaRosa et al (2005) estimate that the amplitude of the large-scale magnetic field is 10 $\mu$G. However, this assumes that the electrons which are (assumed to be) synchrotron radiating fill 100% of the region: LaRosa et al (2005) note that a filling factor of 1% gives a magnetic field amplitude of 100 $\mu$G .

### 9.2.2 Evidence for a *strong* large-scale field

Perhaps the most enigmatic source in the GC region are the non-thermal radio filaments (NTFs) shown in Figure 9.2. The NTFs are long and thin magnetic flux tubes illuminated by synchrotron emission from relativistic electrons that run predominantly perpendicular to the Galactic plane. The main collection of these is called the 'Radio Arc', and is seen in Figure 9.2 as a bundle of filaments which run perpendicular to the plane for a length of $\sim$ 40 pc, but are only 100s of AU wide (Morris & Yusef-Zadeh, 1989). In addition to the Radio Arc, Figure 9.2 shows at least two long filaments which are again parallel to the Galactic plane, but rise far above it. To date, there have been at least 80 such individual filaments detected within GC region (Yusef-Zadeh, Hewitt & Cotton, 2004).

Measurements of the polarised intensity of these filaments at 2 cm ($\nu$ = 15 GHz; Tsuboi et al. 1986) shows that the structure of the magnetic field *within* these filaments is aligned along its length. Furthermore, Yusef-Zadeh & Morris (1987a) places a lower limit to the magnetic field of the NTFs of $\sim$ 1 mG using dynamical arguments. The linearity of the filaments, when the surrounding interstellar medium is inhomogeneous and dynamically unstable requires that the NTFs have to be rigid, and to supply the required rigidity, a magnetic field strength *for the filaments* of 1 mG is needed. Additionally, some filaments (such as those to the north in Figure 9.2) show slight bending. Yusef-Zadeh & Morris (1987a)

argued that this was due to the collision with the "40 km $s^{-1}$" cloud. Equating the ram pressure of the cloud to the magnetic field pressure results in a magnetic field value of at least 1 mG.

The fact that these objects, having such a strong magnetic field, appear to be static is used to imply that a similarly strong, large-scale magnetic field pervades the region, lest the NTFs dissipate over short time scales because of the large internal magnetic pressures created. Finally large-area, single dish polarimetric observations of the region have shown that there is large scale, magnetic structures extending to at least ±110 pc from the Galactic plane (Tsuboi et al., 1986), suggesting the presence of a large scale, ordered magnetic field.

## 9.3 Measuring the Galactic centre magnetic field amplitude

Given that the dynamics of the gas and relativistic particles within the GC region is highly dependent on the amplitude of the large-scale magnetic field (Morris & Serabyn, 1996), and that Sections 9.2.1 and 9.2.2 show that separate pieces of observational evidence imply that the amplitudes are very uncertain, it is extremely important to possess precise information on the magnetic field amplitude.

Given that Section 9.2.2 outlined evidence that the large-scale magnetic field amplitude of the GC region is strong, then any synchrotron emission will, in the presence of such strong fields, exhibit a 'spectral break'. A spectral break – as will be shown below – selects magnetic field and density configurations which, because of a lack of corresponding GeV $\gamma$-ray emission, provides a lower limit to the magnetic field amplitude of 100 $\mu$G . In the next section, we outline the theoretical case for a spectral break.

### 9.3.1 Origin of a spectral break

Chapter 4 outlined the theory of how ~ GeV electrons and positrons can be created in interactions of cosmic rays with ambient matter. In the presence of the magnetic field amplitudes being considered here, electrons and positrons at $1 - 10$ GeV energies will radiate synchrotron photons at GHz frequencies.

It was also shown in Chapter 4 that the cooling processes of most importance were (apart from synchrotron emission), ionization, bremsstrahlung and inverse-Compton scattering. Specifically, it was shown that the relative importance of bremsstrahlung and synchrotron emission is dependent on the different values of (i) the magnetic field and (ii) the ambient matter density. The exact values of the ambient density and magnetic field amplitudes determine, for a charged particle at a given energy, whether it cools primarily via bremsstrahlung or synchrotron emission.

For bremsstrahlung emission, the cooling rate, $dE/dt$, is proportional to the energy of the electron, $E_e$, and the ambient hydrogen density, $n_H$ (i.e., $dE/dt \propto E_e \times n_H$), whilst for synchrotron emission, the cooling rate is proportional to the square of the energy and magnetic field amplitude (i.e., $dE/dt \propto E_e^2 \times B^2$). This leads to a change in slope of the (cooled) electron spectrum by 1 as the cooling mechanism switches from bremsstrahlung to synchrotron with increasing energy. There is, then, a mirroring change in the synchrotron spectrum of $1/2$ in spectral index, that is, a so-called *spectral break*. We note here that the spectral break in this instance is specific to a downturn in a radio continuum spectrum which is due to the cooling of electrons in a magnetic field. This is different from other spectral break, such as that due to synchrotron self-absorption (which occurs in the opposite sense: the spectral

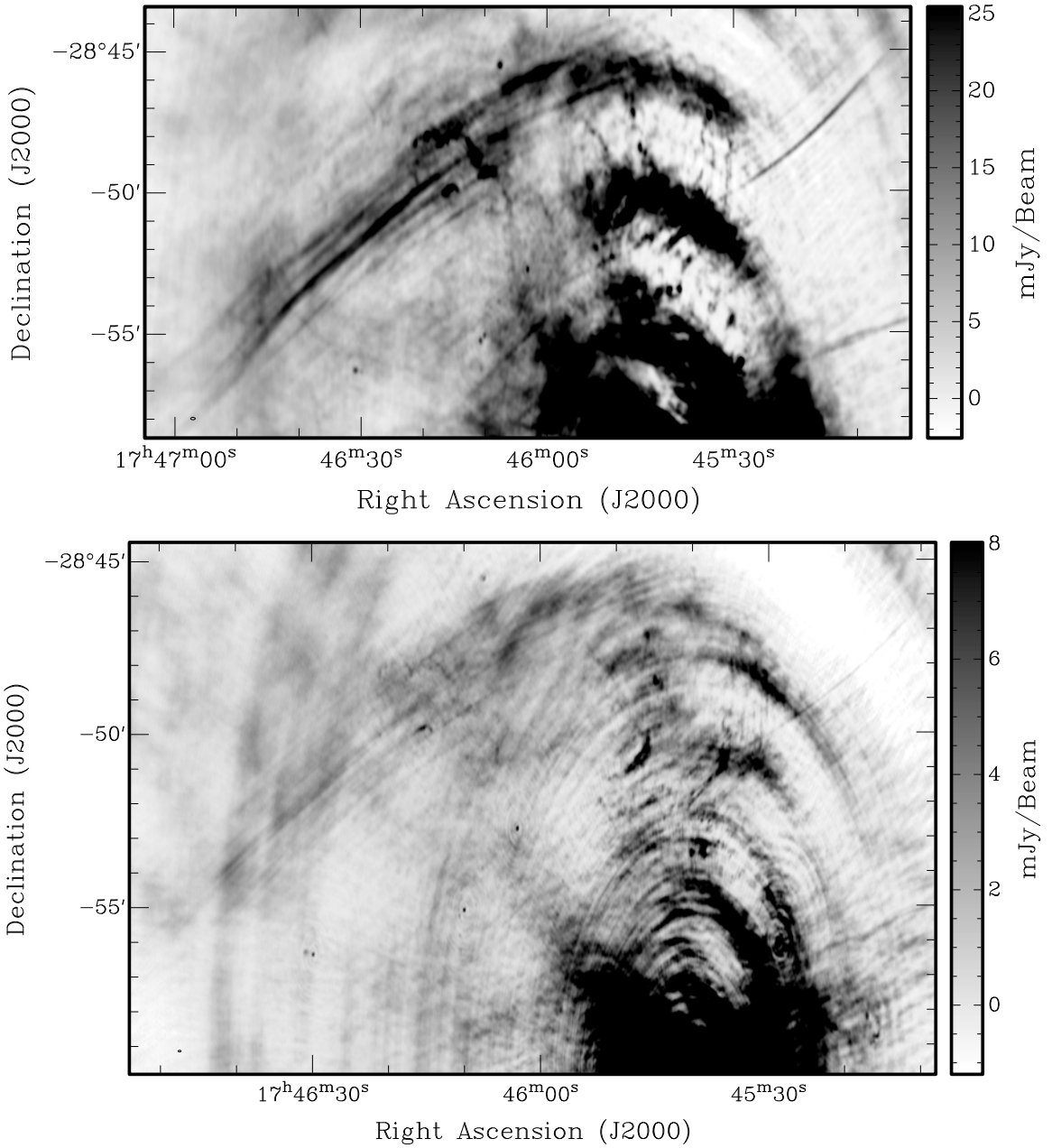


Figure 9.2: A view of the Radio Arc and non-thermal radio filaments at 1.4 GHz (*Top*) and 2.4 GHz (*Bottom*) made with 210 m and 6C configuration ATCA data – a subset of the data used in Chapter 7 – at a resolution of $\sim 2'' \times 3''$ illustrated by the beam in the lower left-hand corner. That the filaments are not as intense at 2.4 GHz illustrates their non-thermal nature (note the differences between the intensity scales on the right hand side of each images: the 2.4 GHz image is shown at a lower intensity level). It should also be noted that these images have not been corrected for the attenuation due to the primary beam response.

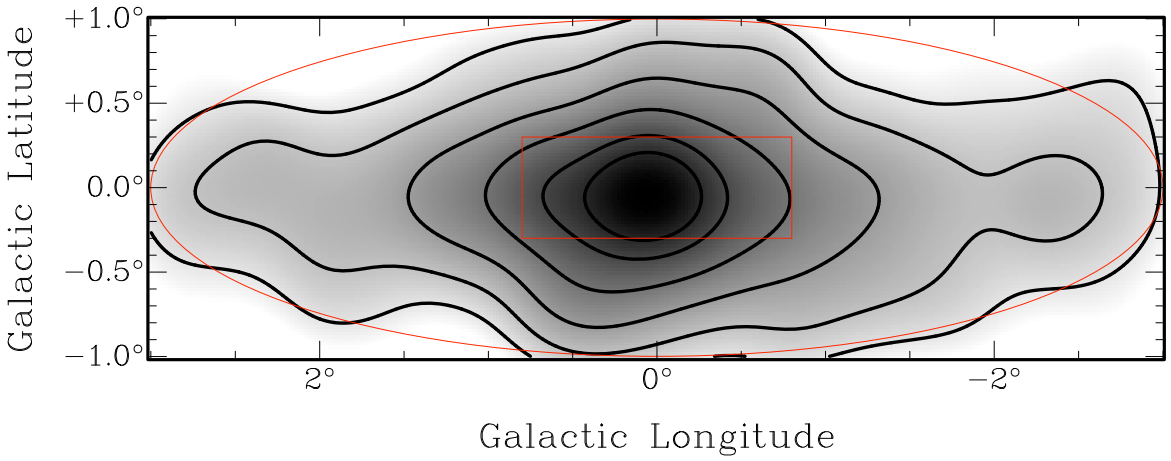


Figure 9.3: Total intensity image from Handa, et al. (1987) of the DNS at 10 GHz convolved to a resolution of $1^\circ.2 \times 1^\circ.2$ with contours at: 10, 20, 40, 80, 160 and 240 Jy/beam. There is a striking constancy in the appearance of the DNS from 74 MHz to at least 10 GHz (the large red ellipse traces the region which LaRosa et al (2005) identified as the 'DNS' on the basis of their 74 and 330 MHz observations). The small red rectangle delineates the region from which, on the basis of TeV observations, the HESS collaboration derives a diffuse TeV $\gamma$-ray intensity (Aharonian et al, 2006).

index becomes positive), or due to a break in the injected particle distribution, such as modeled using an exponential cutoff, which as discussed below, is not expected until much higher frequencies.

This hypothesis is complicated, however, by the fact that a spectral break does not solely select magnetic field values: it selects both magnetic field amplitude and ambient hydrogen density. Thus if one observes a break in the radio spectrum at frequency $\nu_{bk}$, then this will in general be a function of magnetic field amplitude and density: $\nu_{bk} = \nu_{bk}(n_H, B)$.

## 9.4 Radio data

We assembled single dish data at 1.4, 2.4, 2.7, 8.35, 10 and 14.35 GHz (Reich et al (1990); Reich et al. (1984); Duncan et al. (1995); Langston et al. (2000); Handa, et al. (1987); Langston et al. (2000) respectively) in addition to the 74 and 330 MHz data points supplied by LaRosa et al (2005). Comparison of Figure 1(c) of LaRosa et al (2005) with Figure 9.3, shows that emission on sizes of the DNS exist from 74 MHz up to at least 10 GHz. At GHz frequencies, various background emission will pollute the intensity of the DNS, hence before the flux densities of the DNS could be integrated, we had to remove the various backgrounds.

## 9.5 Background emission and subtraction

Given that the contribution from extragalactic sources to the total radio fluxes is negligible (e.g., $\lesssim$ 15 Jy at 1408 MHz for the entire DNS region; Bridle 1967), there are two potentially significant backgrounds/foregrounds to be considered in arriving at a flux attributable to the signal from diffuse, large-scale synchrotron emission

### 9.5.1 Line-of-sight Galactic plane synchrotron background/foreground

The most important background emission for which an account has to be taken is the synchrotron emission due to free electrons within the Galaxy: the Galactic synchrotron

background (GSB). We normalized the GSB at 408 MHz via recourse to the Galactic plane survey of Haslem et al (1982) and, following the procedure of LaRosa et al (2005), chose a constant longitude slice free of discrete sources (well outside of the DNS) near $l = 354°.5$ to measure the latitude dependence of the 408 MHz flux normalization. The latitude dependence is shown in Figure 9.4, which shows the intensity (in non-standard units of Jy beam$^{-1}$ ) as a function of Galactic longitude. The longitude dependence was modeled using a two component Gaussian distribution consistent with a broad distribution (FWHM$\sim$ 15°) and a narrow distribution (FWHM$\sim$ 5°). At higher frequencies we expect the GSB to have a spectral index (SPIN) of $\alpha = -0.695 \pm 0.120$ (Platania et al. (2003); assuming $I_\nu \propto \nu^\alpha$). The GSB is expected to display a break at a frequency of $\sim$ 22 GHz (Völk, 1989), well above the region where we are fitting.

As we cannot directly measure the GSB at higher frequencies due to the presence of other backgrounds, *we leave the GSB spectral index as a free parameter in our fitting.*

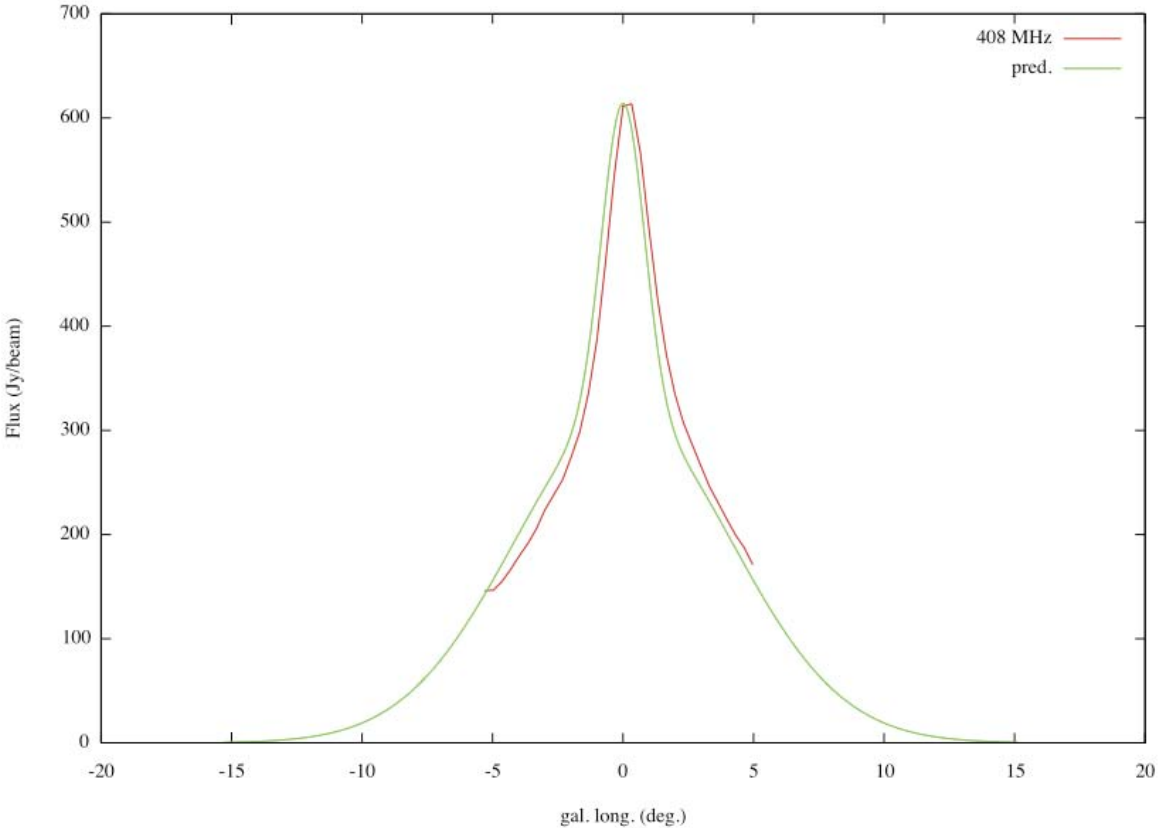


Figure 9.4: Cross-section of 408 MHz emission (red line) at $b = 354°.4$, as per LaRosa et al (2005). Also shown is the emission as modeled using a two-component Gaussian distribution (green). The difference between the model and the 408 MHz emission is due to the peak in the 408 MHz emission not being symmetrical about the Galactic plane. It should be noted that this will have a negligible effect on the background subtraction.

### 9.5.2 Discrete source background

As described below, LaRosa et al (2005) measured a $\sim$ 1000 Jy flux at 330 MHz attributable to discrete sources with the VLA (LaRosa et al., 2000). These measurements were performed in an array configuration sensitive to emission out to a scale of $\sim 1°.2$. We have used a technique based on Fourier decomposition (described below) to obtain the flux contribution of discrete sources up to this same angular scale for the higher-frequency, single dish data.

We note that including emission out to angular scales of $\sim 1^{\circ}.2$ within the discrete source background is highly conservative and, in particular, should capture almost all thermal emission, even that due to extended, low density HII regions (Schmidt, 1978).

In order to confirm our small-scale fluxes, we have used unsharp masking (Sofue & Reich, 1979), convolving to the same angular scale of $\sim 1^{\circ}.2$.

The discrete source spectrum (shown by the lower data points which remain unfitted in Figure 9.10 of Section 9.7) approximately describes a power-law with spectral index of $\alpha = -0.38 \pm 0.07$ consistent with the expectation that the discrete sources in the field are a mixture of non-thermal ($\alpha = -0.7$), optically thick free-free ($\alpha = 2$), and optically thin free-free ($\alpha = -0.1$) emitters (as observed by Law et al (2007) at 5 and 8.5 GHz for a smaller field).

### 9.5.3 Discrete background subtraction method: Fourier Analysis

LaRosa et al (2005) uses a combination of single-dish and interferometric observations at 74 and 330 MHz to establish the existence of a diffuse non-thermal source (DNS) at the Galactic centre (GC). They exploit the nature of the interferometer as a spatial filter to estimate the amount of flux from this region which is due to small-scale sources. Subtracting this small-scale flux from the single-dish observations, they arrive at a flux density which they claim is solely due to the DNS (once the GSB has been subtracted).

Here we outline the analysis which we have undertaken to produce a spectrum which is consistent with LaRosa et al (2005), and which we extend up to a frequency of 10 GHz.

Radio interferometers such as the Very Large Array (VLA), will act as a spatial filter. This occurs when radiation which is emitted on characteristic scales larger than that representing the approximate angular scale of the smallest baseline separation of two antennae and the emission will not be reconstructed in image deconvolution. It is for this reason that it is common practice when imaging structures on large scales, to add the information filtered by the interferometer using single-dish observations (Stanimirovic (2002); see Chapters 6 and 8 for example).

The effect of spatial filtering is illustrated in Figure 9.5 (*Top*) which shows the total flux as a function of ($uv$)-spacing for VLA and Australia Telescope Compact Array (ATCA) data of the region within the DNS at 330, 1384 and 2368 MHz (LaRosa et al. (2000) for the 330 MHz VLA data and Jones et al (2008a) for the 1384 and 2368 MHz ATCA data). This shows that approaching the smallest $uv$-spacings (largest angular scales), the total flux in the image is curtailed as the interferometer begins to filter the emission. This is in contrast to plot on the right, which shows 2.4 GHz ATCA data (green line) and 2.4 GHz Parkes data, which shows that at small $uv$-spacings, the single-dish flux continues to increase at larger angular scales, whereas the amount of emission – according to the ATCA – doesn't increase.

For the VLA, using the most compact configurations, this is $\sim 4200''$[1], which corresponds to $50\lambda$, since $u = \lambda/b = 1/R = 1/0.02 = 50\lambda$, where $b$ is the baseline of the interferometer, $\lambda$ is the wavelength and $R$ is the resolution in radian ($4200'' = 0.02^{c}$). Hence the $\sim 1000$ Jy of flux estimated by LaRosa et al (2005) is obtained from an angular scale of $50\lambda$. Note that this shows that the total flux for the DNS will lie at $\sim 10\lambda$ – as Figure 9.6 shows, this roughly corresponds to the total fluxes obtained by integrating over the area of the DNS – implying that the units and scaling applied to the images are correct. Additionally, taking

[1] http://www.vla.nrao.edu/astro/guides/vlas/current/node9.html

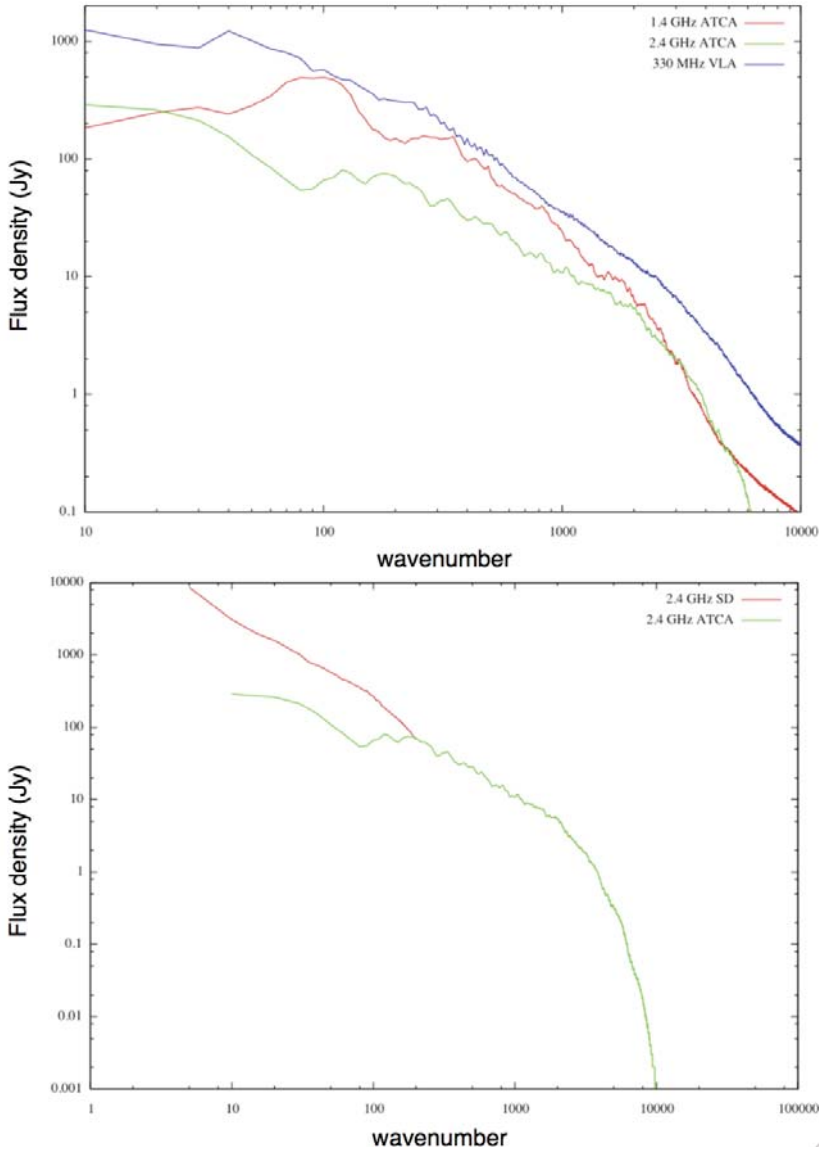


Figure 9.5: *Top:* Fourier transform of the VLA and ATCA images at 330, 1384 and 2368 MHz from LaRosa et al. (2000) and Jones et al (2008b) respectively. The y-axis is flux in Jy, and the x-axis is in units of $\lambda$, as described in the text. *Bottom:* A plot of the flux against angular scale for the ATCA-only data at 2368 MHz and the PKS-only at 2.4 GHz Duncan et al. (1995), illustrating the continuity of the flux density.

the logarithmic ratio of the fluxes to the frequencies one would gain the spectral index of the emission at a given angular scale.

In order to obtain fluxes which are consistent that all frequencies as well as for both interferometric and single-dish data, we derived the following algorithm:

1. The data was regridded and convolved to the same grid and resolution as the 330 MHz VLA data. The single-dish data was regridded and convolved to the grid and resolution of the PKS 2.4 GHz data. Every image was also regridded into J2000 coordinates.

2. The location of the central pixel in all images was changed to that corresponding to ($l$,$b$)=(0,0) for all images.

3. Each image was divided by the number of pixels per beam using the MIRIAD task *maths*, so that each pixel value is Jy/pixel. The number of pixels per beam was

calculated by dividing the beam area ($A_b = 1.133(\Omega_a \times \Omega_b)$) by the area of each pixel, where all units are in arcseconds.

4. The MIRIAD task *fft* was then used to take the Fourier transform of every image. The FT of the intensity in Jy/pixel is simply Jy (Dickey et al., 2001).

5. The MIRIAD task *ellint* was used to take the average flux in annuli of increasing radii from the centre of the ($uv$)-plane

6. The total flux in the image at each frequency is then the flux which is at a corresponding radii as that in the 330 MHz VLA FT plot.

Figure 9.6 shows a plot of flux density in Jy, against angular scale for all the single-dish images we posses. This shows that the emission at all size-scales follow an unbroken power-law. The flattening (at the largest angular scales) of the 1.4, 2.7 and 10 GHz images is due to the finite size of the images (except for the 2.4 GHz image, which is larger). The slight downturn at the smallest angular scales is due to reaching the resolution of the 2.4 GHz image (which is the worst resolution image, to which all other images have been convolved). Note that at all angular scales that the emission is non-thermal.

Finally, we note that, since an interferometer strictly measures only a lower limit to the flux, then the small-scale flux derived here would be an upper limit if the small-scale flux found by the VLA in LaRosa et al (2005) is not equal to the total flux on these size scales as measured by a single dish at 330 MHz. This situation does not alter out detection of a spectral break, given that the break is still statistically robust from the integrated fluxes (c.f. Section 9.7).

### 9.5.4 Discrete background subtraction method: Unsharp Masking

In order to obtain a better understanding of how well the Fourier analysis works, and to gain an insight about the errors from this analysis, we also employed a technique known as unsharp masking (UM). UM is a technique that was first adopted to enhance nebulous emission in optical astronomy images by Malin & Zealey (1979). It has since been used in a wide variety of (not just astronomical) applications, and works by subtracting out low spatial frequency emission. Thus, not having the original with which to filter the large scale emission (such as with the VLA and ATCA data described in the previous section), this technique allows us to estimate the emission on small scales without recourse to interferometric data.

There have been a large number of UM filters developed, however, we used a technique based in that developed for single-dish radio observations by Sofue & Reich (1979). In the previous section, it was shown that the VLA filters emission from scales larger than $4200'' \sim 1.22°$, from which LaRosa et al (2005) derived a small-scale flux density of $\sim 1000$ Jy. Thus we chose a filter of this size-scale with which to perform the UM. Below we describe the algorithm, for which an example of the images before and after are shown in Figure 9.7.

1. All images were converted to Jy/beam units, if appropriate using the standard formula:

$$S_\nu = \frac{2kT_B\nu^2\Omega}{c^2} = \frac{\nu^2 T_B \theta^2}{1.222 \times 10^6} \tag{9.3}$$

where $S_\nu$ is the flux density in units of Jy beam$^{-1}$ , $k$ is Boltzmann's constant, $T_B$ is the brightness temperature in K, $\nu$ is the frequency, $\Omega$ is the solid angle of the beam in

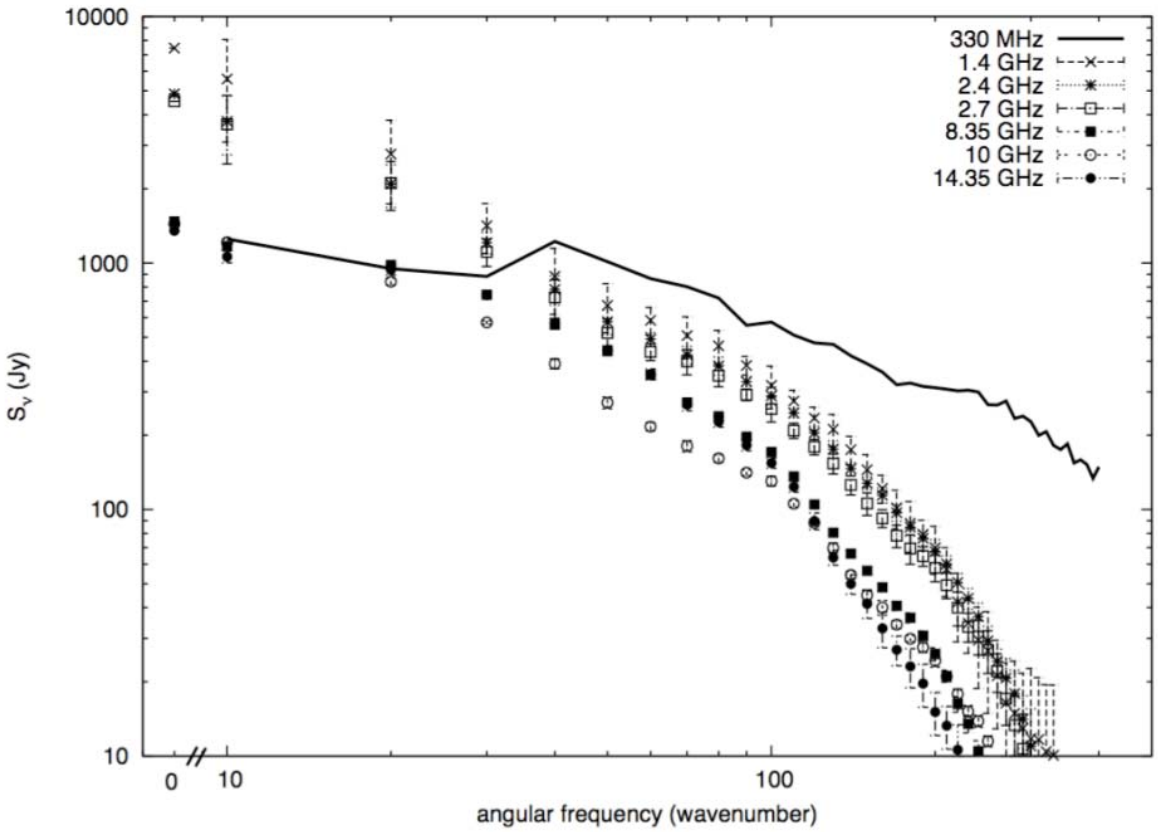


Figure 9.6: Flux as a function of angular scales for the single dish data as labelled in the legend and produced (with errors) following the method described in the text. The (black) solid line is the flux density as a function of wavenumber of the 330 MHz datum from LaRosa et al (2005).

steradians, $c$ is the speed of light, $\theta$ is the FWHM of the telescope beam, and $1.222\times10^6$ is a conversion factor, taking into account the beam volume and the conversion from arcseconds to steradian.

2. Each blank pixel in the images were converted to be 0.0, since the MIRIAD task *convol* doesn't deal well with blanked images. Each image was then convolved to the masking beam width (FWHM=4200″). This image is known as the MASK.

3. Each image (original and mask) was then converted to brightness temperature (in K) using the inverse of the above equation.

4. The original image had the mask subtracted from it, creating a residual image.

5. An image was created by taking the original image from the residual image if the difference is less than (or equal to) zero, and the mask image where the residual is (strictly) greater than zero. This map is then convolved to the mask resolution to create a BACK map - representative of the large scale emission.

6. The BACK map was then subtracted from the original map to create the SOURCE map, which contains emission on size scales smaller than the mask.

7. The BACK and SOURCE images were then converted back to Jy beam$^{-1}$ units.

8. The MIRIAD task *imstat* was used to derive flux densities within the DNS only (via the region keyword).

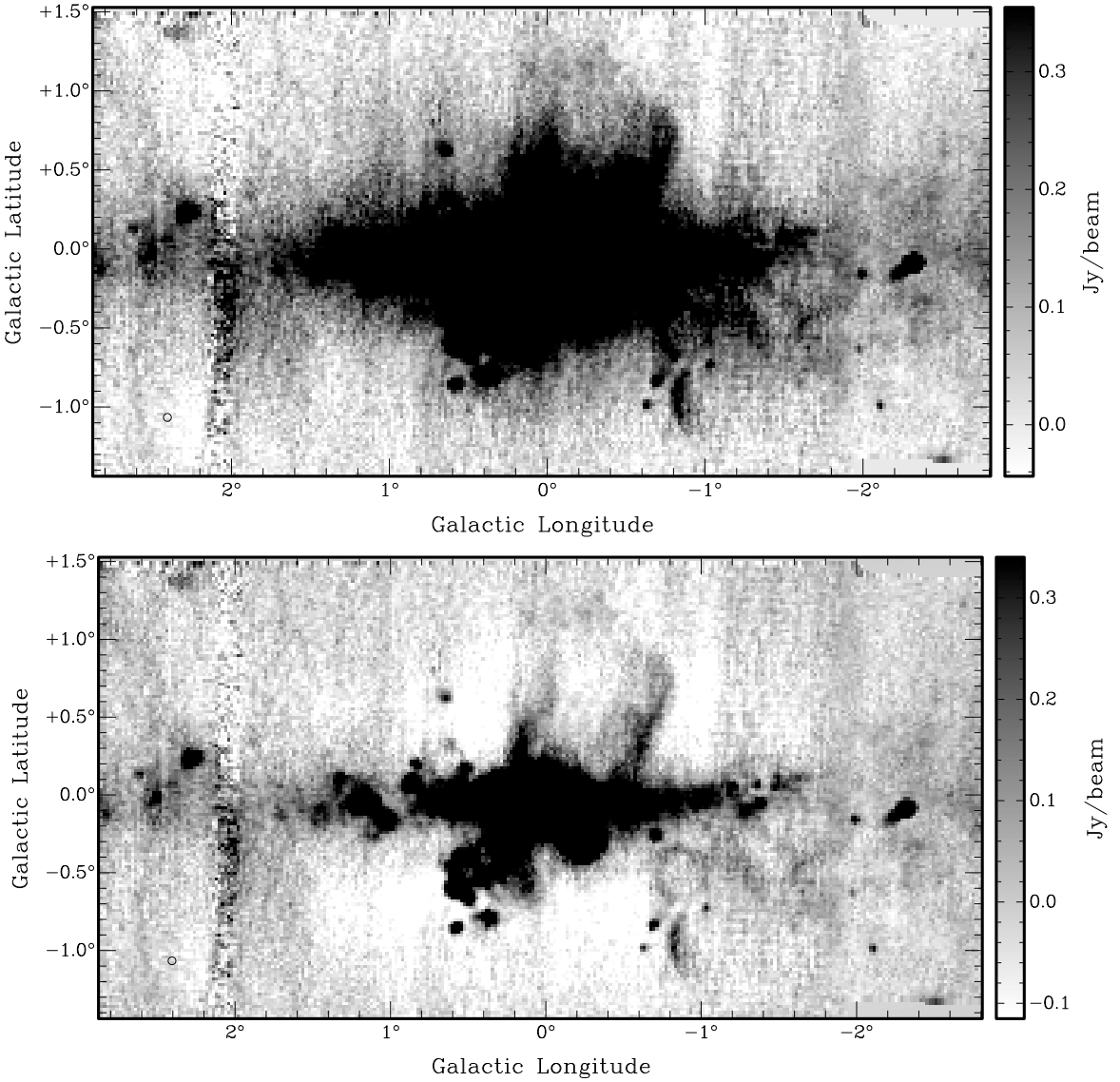


Figure 9.7: The DNS before (*Top*) and after (*Bottom*) the application of the UM technique at 10 GHz with a 1°.2 FWHM beam. Note that the large scale emission is absent from the (*Bottom*) image, and a number of point sources are much more evident (such as the Radio Lobe and the SNRs G359.1-00.5 and G359.0-00.9).

Figure 9.7 is the result of this masking technique for the Nobeyama 10 GHz data. It shows that the UM routine uncovers the small scale emission very well, although the errors in the image which are present at all angular scales (such as the noisy stripe in the 10 GHz data shown in Figure 9.7) are not affected by the algorithm.

In order to check of the validity of the filter aspect of the UM technique, and the accuracy of the Fourier Analysis technique outlined above, we implemented two checks of the data. Firstly, we performed the algorithm using a mask which is equal to the resolution of the image. Using the formalism of Sofue & Reich (1979) one expects to get a zero map (i.e., all the emission is filtered out). Performing the algorithm as described above results in such a zero-map being produced. Additionally, if one masks with a mask the size of the DNS, then one expects to get the flux density of the DNS derived from other means (such as direct integration, such as was described above). Performing the algorithm described above resulted in flux densities being obtained which are consistent with direct integration of the DNS at each frequency. Thus we conclude that the algorithm described above is

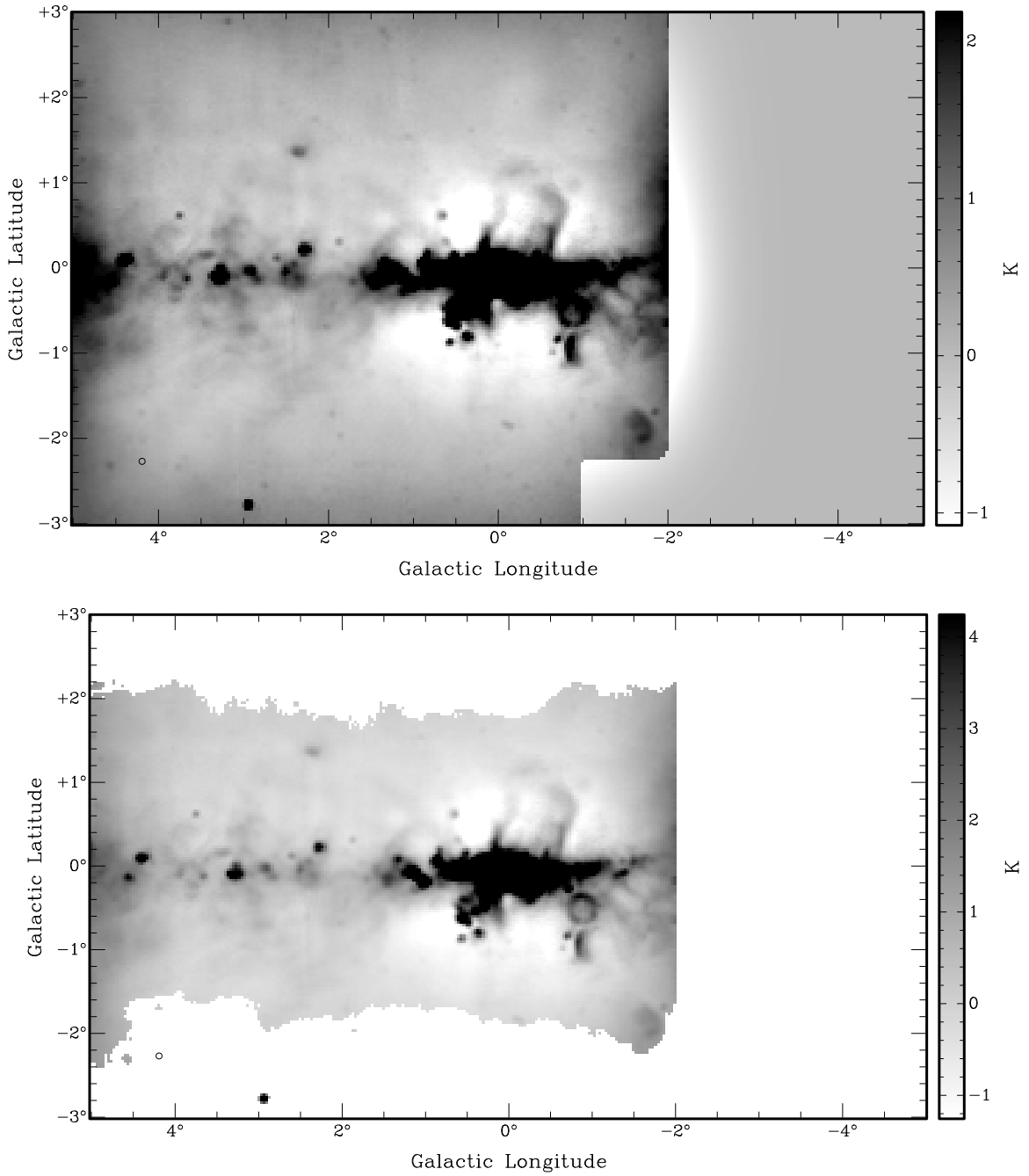


Figure 9.8: Result of the UM technique for the 2.7 GHz Efflesberg data using no noise masking (*Top*) and a noise mask of 2 K (*Bottom*). Note the increased noise created at the edge of the image, which is absent when the noise masking is performed.

quantitatively consistent with a Fourier filter for emission above size-scale of the masking beam.

Finally, in the derivation of the small-scale fluxes, it is important that one checks for effects which can alter the fluxes. Since we are asking the UM technique to act like a filter in the Fourier domain, it is necessary to check whether this is occurring. Additionally, the UM technique is known to introduce noise into an image at the edge of the image. This is especially true in the case of the DNS, since we are using a Gaussian filter for emission which can best be described using two Gaussian distributions (c.f. Section 9.5.1).

For flux density determinations, the noise in the image which is introduced because of the algorithm was masked out as in Figure 9.8. The level of this mask was determined by

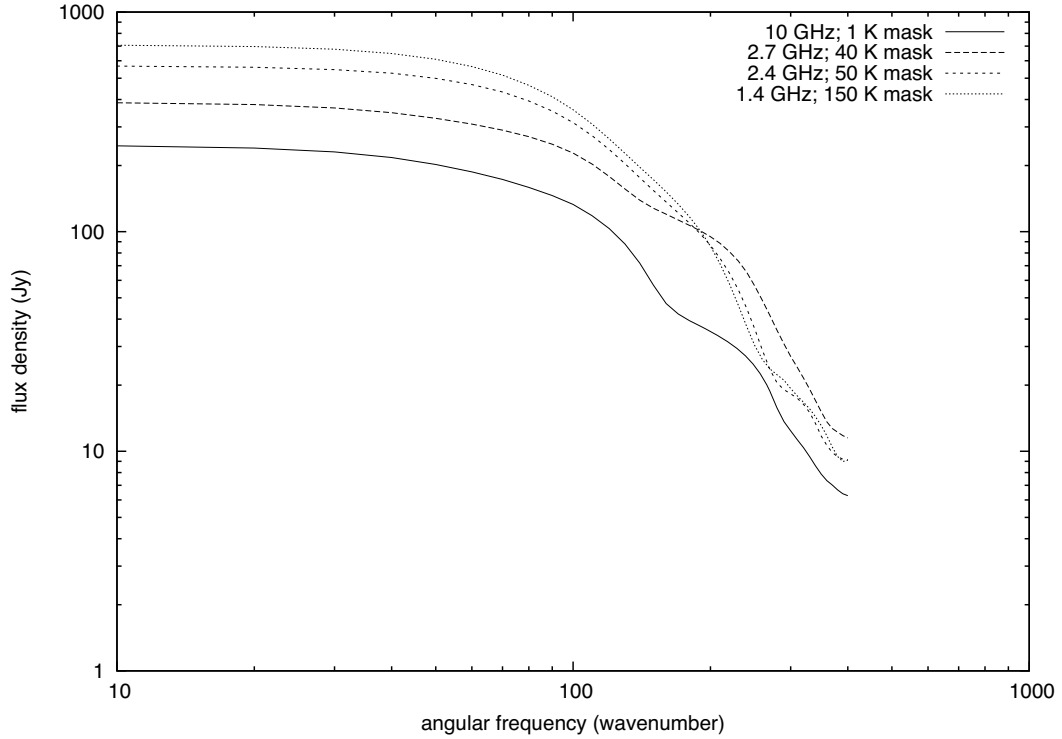


Figure 9.9: Flux as a function of angular scales for the single dish data as labelled in the legend and produced following the method described in the text.

the same Fourier analysis as described above, such that the masking level produce a flat Fourier profile above a spatial frequency of 50.

The result of this is shown in Figure 9.9, however, because the level of the mask is arbitrary (although it does result in small scale fluxes which closely match the Fourier Analysis results and direct integration) and higher-level masks can produce a flux which has relied upon a region smaller than the DNS, we have not used these numbers in our analysis more than to check the validity of the Fourier analysis technique. We suggest that this method is not independent enough of the mask level to provide robust flux density estimates in such complex regions (although it *may* be suitable for use in less complex regions outside the Galactic plane).

## 9.6 Errors

The errors for all radio fluxes in this paper have been determined as follows:

1. The 74 MHz datum has an error for the *total* DNS flux of 1000 Jy (LaRosa et al, 2005).

2. At 330 MHz, we adopt an error of 5% from Law et al (2007).

3. We assume 10% errors at 1.4 and 2.7 GHz, since these images adopt absolute zero measurements from the 408 MHz images of Haslem et al (1982) and 10% is nominated as the systematic error in the latter.

4. At 2.4 GHz we adopt a 6% error from Haynes et al. (1992) (who describe observations of the same region with the same telescope but at 5 GHz). At 10 GHz we adopt an error of 7% from Sofue et al. (1983) (who describe observations of a different region, but at the same frequency and with the same telescope).

5. For the discrete sources fluxes obtained from Fourier analysis of single-dish data, we obtained a conservative error estimate by chosing as large a region as possible that was below the Galactic plane, common to all maps, and containing of no significant emission features (no discrete sources, little Galactic plane emission). We derived the Fourier spectrum of this region at each frequency to estimate the amount of power in any given region attributable to RMS noise fluctuations. We scaled the total flux at a wavenumber of 50 from the noise region by the relative size of the DNS to give the error on DNS discrete source flux, which are shown as the error bars in Figure 9.6.

## 9.7 Evidence for a spectral break

Having outlined above the methods for the subtraction of the sources of background emission, the radio continuum spectrum for the DNS from 74 MHz to 10 GHz was compiled, which is shown in Figure 9.10. The 74 MHz datum does not have a GSB component because of the same spatial filtering described above, and because of the low frequency emission being absorbed by intervening HII regions. The 0.3, 1.4, 2.4, 2.7 and 10 GHz fluxes are represented by circles (and associated error bars due to the errors described above). The (blue) long-dashed line is the spectrum due to small scale emission as determined from the Fourier analysis and unsharp masking methods.

Fitting separate power laws to, respectively, the lower three and upper three radio data, we find that these extrapolations intersect at ~1.6 GHz and, moreover, the power-law fitted to the higher-frequnecy data has a best-fit spectral index steeper by $\sim 0.6$ than the lower-frequency one, strongly suggestive of a spectral break due to synchrotron cooling (as we now explain).

Although the data *a priori* is strongly suggestive of a spectral break, we have modeled the DNS radio continuum spectrum as a pure power-law, fitting the model using a $\chi^2$ fitting procedure. This attempts to fit the normalization and spectral index of the data to the 74 MHz datum *and* the identical power law + GSB power law (with normalization determined at 408 MHz but variable spectral index; we account for a contribution from the GSB spectral index in the $\chi^2$ function) to the 330 MHz datum and higher frequency data we have assembled. The single power law is represented in Figure 9.10 as the (red) dotted line. We find a minimum $\chi^2$ of 5.2 per degree of freedom (for 2 degrees of freedom) and can excluded the null hypothesis at greater than 98% confidence.

We then attempted to fit a spectrum of *cooled* electrons to the same DNS data. The free parameters for fitting this spectrum are the magnetic field, ambient hydrogen density and the spectral index of the parent particle population and the result of fitting the radio spectrum to these parameters is shown in Table 9.1. This shows (1) the magnetic field, (2) the resulting $\chi^2$value for the parameters in the following columns, (3) $n_H$ (with the superscript and subscript indicating the largest and smallest $n_H$ values, respectively, satisfying a reduced $\chi^2 \sim 1$ – subsequent super- and subscript values of other parameters give the best fits at these extrema of the acceptable $n_H$ range), (4) spectral index *at injection* of the emitting electron population (see Crocker et al. (2007) for details), (5) the best-fit filling factor and

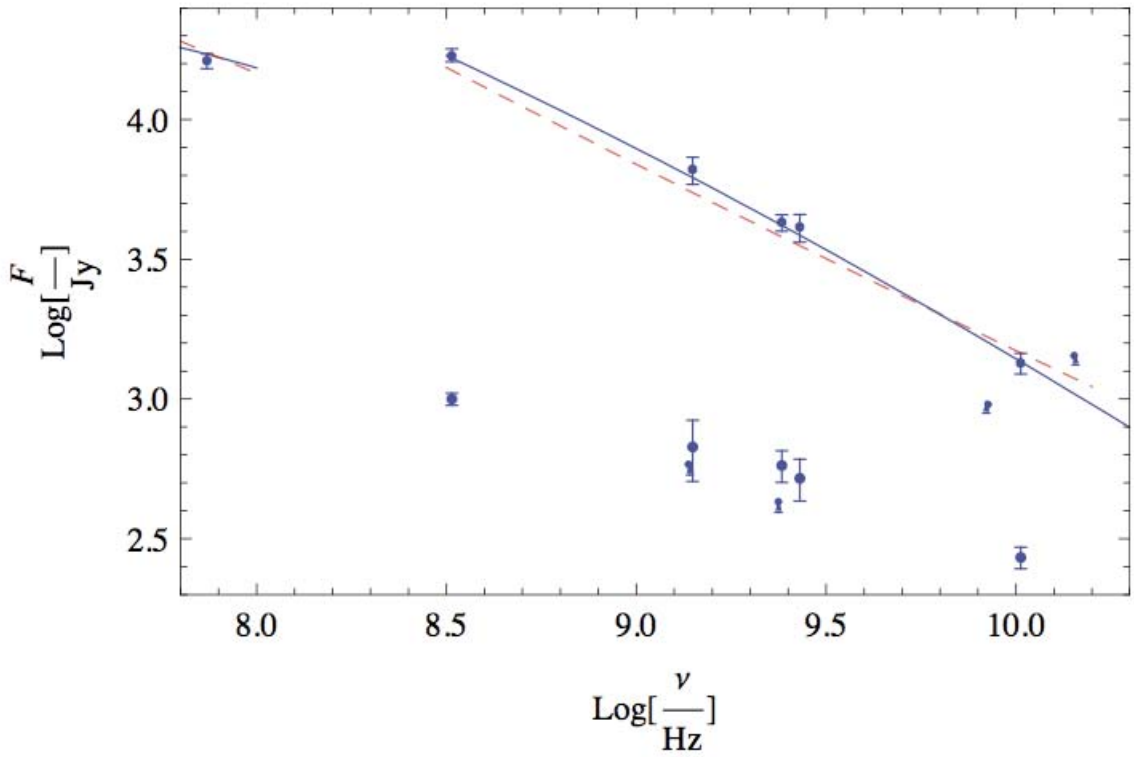


Figure 9.10: DNS radio spectrum (LaRosa et al 2005; Reich et al 1990; Reich et al. 1984; Duncan et al. 1995; Langston et al. 2000; Handa, et al. 1987) data and models. The 74 MHz datum does *not* include a contribution from the Galactic plane synchrotron foreground/background (GSB). All other flux data *do* include GSB, but have had contributions due to discrete sources with angular scales $< 1^\circ.2$ removed from them (appearing as the flux data points at ≤1000 Jy which have *no* fitting). Fluxes at 8.35 and 14.35 GHz represent lower limits (Langston et al., 2000) because these data have been processed with a median filtering technique that reduces the flux measured on scales larger than 34'. The upbreak above 10 GHz is due to spinning dust (Finkbeiner et al., 2004) and, consequently, the 14.35 GHz lower limit is not a constraint for our fitting. The solid line represents the best-fit *sum* of the flux due to our model (synchrotron emission from a cooled electron distribution) **plus** GSB for the case of a 100 $\mu$G field. The sum of model flux plus GSB (with fitted spectral index) is fitted to all data at frequencies ≥ 330 MHz; the signal *alone* is fitted to the 74 MHz datum (hence the discontinuity in the curves). The red dashed curve represents the best-fit obtained for the null hypothesis case of a radio signal represented by a pure power law plus GSB contribution (above 74 MHz).

(6) the mass contained within the DNS given the values of $n_H$ and $f$. For this calculation, we have included losses due to inverse-Compton emission by the electrons colliding with the ambient light field (which has a volumetric average energy density of 13 eV cm$^{-3}$ given the $2.5 \times 10^9\ L_\odot$ stellar luminosity of the nuclear bulge (Laundardt et al, 2002).

Table 9.1 shows that a field of $\gtrsim 100\mu$G is required in order to get a good fit to the data. As we now explain $\gamma$-ray data can be used to put this constraint on a firm footing.

## 9.8 A lower limit to the large-scale magnetic field

### 9.8.1 Broadband spectrum of the DNS

Figure 9.11 shows the broadband spectrum for the DNS region. Specifically it shows the flux density as a function of energy from the $\sim 10^{-7}$ eV energies of the synchrotron radiating photons (blue solid and dashed lines) of the GeV electrons, to the TeV energy emission

| $B$ (G) | $\chi^2/d.o.f.$ | $n_H$ ($cm^{-3}$) | $\gamma$ | $f$ | $M_H$ ($M_\odot$) |
|---|---|---|---|---|---|
| (1) | (2) | (3) | (4) | (5) | (6) |
| $1.0\times10^{-5}$ | 2.8 | $12^{15}_{9}$ | $2.0^{2.0}_{2.0}$ | $1.8\times10^{-2}$ | $5.2\times10^{5}$ |
| $3.2\times10^{-5}$ | 2.4 | $17^{39}_{12}$ | $2.0^{2.0}_{2.0}$ | $1.3\times10^{-2}$ | $5.4\times10^{5}$ |
| $1.0\times10^{-4}$ | 1.1 | $49^{660}_{23}$ | $2.0^{2.3}_{2.0}$ | $5.4\times10^{-3}$ | $6.7\times10^{5}$ |
| $3.2\times10^{-4}$ | 0.34 | $140^{650}_{59}$ | $2.1^{2.3}_{2.0}$ | $2.5\times10^{-3}$ | $9.3\times10^{5}$ |
| $1.0\times10^{-3}$ | 0.13 | $360^{2700}_{160}$ | $2.1^{2.4}_{2.0}$ | $1.5\times10^{-3}$ | $1.4\times10^{6}$ |

Table 9.1: Best-fit parameters from fitting a model of a cooled, synchrotron-emitting electron population to the ~GHz radio emission from the the DNS within the assumed $B$ amplitude listed in column 1. The $n_H$ values in superscript and subscript are the largest and smallest, respectively, that satisfy $\chi^2/dof \lesssim 1$, and the sub- and superscript values of $\gamma$ are those corresponding to these $n_H$. Note that $\gamma$ has been constrained to lie in the range 2.0–2.4.

produced by bremsstrahlung and inverse-Compton emission (purple solid and dashed lines) with a magnetic field amplitude of 30 $\mu$G (dashed lines) and 100 $\mu$G (solid lines). Importantly it shows two upper limits at GeV and TeV energies, which are also highlighted in Columns (5) and (6) of Table 9.2 respectively. These upper limits were obtained in the following ways:

1. Observations of the GC region by the EGRET telescope (Meyer-Hasselwander, et al., 1998; Pohl, 2005) allow the estimation of a conservative upper limit to the GeV intensity $\gamma$-ray photons produced via non-thermal bremsstrahlung emission at similar energies to the GHz radiating synchrotron photons.

2. Similar observations of the GC region by the HESS instrument (see Chapter 3 for a detailed discussion of the HESS instrument) revealed diffuse TeV $\gamma$-ray emission over a smaller (than the DNS) region towards the GC. This flux of TeV $\gamma$-rays observed in the region of $|l| < 0.8^\circ$ and $|b| < 0.8^\circ$, but not so far from outside this region, represents another upper limit for the production of $\gamma$-rays via thermal bremsstrahlung of the same (but higher energy) electron population that produces the GHz synchrotron photons, and IC emission on the background photon fields.

### 9.8.2 $\gamma$-ray derived lower limit

Figure 9.11 and Table 9.2 show – and this is the essential point of our analysis – that for the lower magnetic field value of 30 $\mu$G, the upper limits of $\sim 6\times10^{-4}$ cm$^{-2}$ s$^{-1}$ sr$^{-1}$ at GeV energies and $1.4\times10^{-20}$ cm$^{-2}$ eV$^{-1}$ s$^{-1}$ sr$^{-1}$ above 1 TeV described above are violated. *The electrons required to produce (via synchrotron emission) the detected, non-thermal radio signal of the region produce too much $\gamma$-ray emission at GeV and TeV energies (via non-thermal bremsstrahlung emission) unless the magnetic field is $\gtrsim$100 $\mu$G.*

Table 9.2 shows (for the best-fit values derived above and displayed in table 9.1), in the specified column, the following: (1) sampled $B$ field; (2) the magnetic energy density in the given field; (3) the energy density (or pressure) in the turbulent motions of the gas assuming (assuming it is at the best-fit $n_H$ and has a velocity dispersion of 20 km/s typical for GC molecular matter (e.g., Morris 2007); (4) the energy density of the synchrotron-radiating, power-law electron population required to reproduce the observed radio emission; (5) the integral $\gamma$-ray intensity above 300 MeV from the DNS region from bremsstrahlung emission by the synchrotron-radiating electron population in the given $n_H$; and (6) the differential

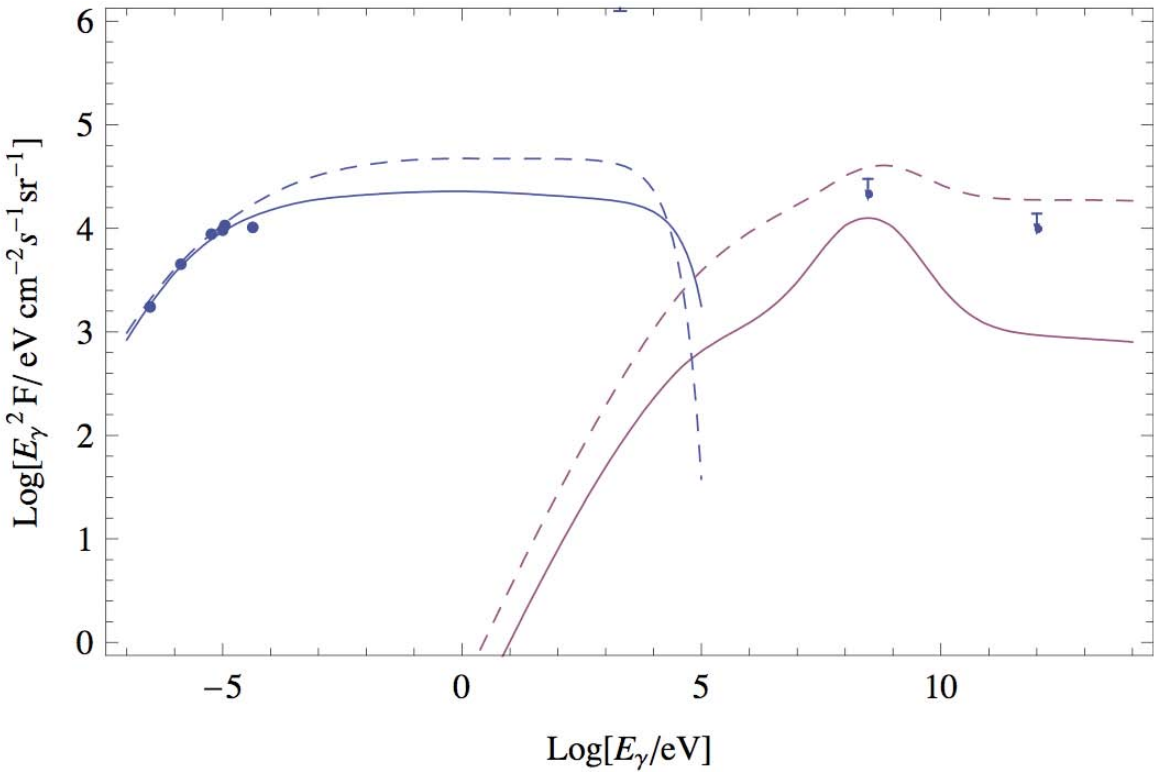


Figure 9.11: Broadband spectrum of the DNS region for magnetic fields of 30 $\mu$G (dashed) and 100 $\mu$G (solid). The injected electron spectrum is assumed to follow a power law (in momentum) up to ~ 100 TeV. The lower energy blue curves are due to synchrotron emission and the higher energy, purple curves due to bremsstrahlung and inverse-compton emission. Note that for field amplitudes in the range 10-1000 $\mu$G, the electrons synchrotron radiating at ~GHz frequencies are bremsstrahlung radiating at ~GeV energies.

| $B$ | $U_B$ | $U_{turb}^{20kms^{-1}}$ | $U_e$ | $\phi_\gamma^{>300\ \mathrm{MeV}}$ | $\frac{d\phi_\gamma}{dE_\gamma}^{>1\ \mathrm{TeV}}$ | $\dot{E}$ |
|---|---|---|---|---|---|---|
| (G) | (eV/cm$^3$) | (eV/$cm^3$) | (eV/cm$^3$) | (/cm$^2$/s/sr) | (/eV/cm$^2$/s/sr) | erg/s |
| (1) | (2) | (3) | (4) | (5) | (6) | (7) |
| $1.0\times10^{-5}$ | 2.5 | $24^{31}_{19}$ | $1.8^{2.2}_{1.4}\times10^{2}$ | $7.2^{9.4}_{5.6}\times10^{-4}$ | $2.2^{2.8}_{1.7}\times10^{-19}$ | $2.1^{2.7}_{1.6}\times10^{38}$ |
| $3.2\times10^{-5}$ | 25. | $35^{81}_{35}$ | $44^{89}_{33}$ | $1.9^{4.4}_{1.4}\times10^{-4}$ | $5.7^{13}_{4.1}\times10^{-20}$ | $6.0^{13}_{4.6}\times10^{37}$ |
| $1.0\times10^{-4}$ | $2.5\times10^{2}$ | $1.0^{14}_{1.2}\times10^{2}$ | $20^{230}_{11}$ | $9.9^{160}_{4.9}\times10^{-5}$ | $2.2^{3.2}_{1.5}\times10^{-20}$ | $4.2^{110}_{2.7}\times10^{37}$ |
| $3.2\times10^{-4}$ | $2.5\times10^{3}$ | $3.0^{14}_{1.2}\times10^{2}$ | $7.5^{30}_{4.7}$ | $5.1^{21}_{2.3}\times10^{-5}$ | $9.7^{4.3}_{7.2}\times10^{-21}$ | $3.8^{17}_{3.0}\times10^{37}$ |
| $1.0\times10^{-3}$ | $2.5\times10^{4}$ | $7.6^{57}_{3.3}\times10^{2}$ | $2.2^{7.8}_{1.6}$ | $2.2^{12}_{1.1}\times10^{-5}$ | $3.6^{1.5}_{3.6}\times10^{-21}$ | $4.6^{19}_{4.7}\times10^{37}$ |

Table 9.2: Various parameters of the DNS region calculated within the assumed $B$ amplitude listed in column (1) and on the basis of the best-fit parameters listed in Table 9.1. Quantities in superscript and subscript are for fits obtained with the largest and smallest $n_H$ that satisfy $\chi^2/dof \lesssim 1$.

$\gamma$-ray intensity at 1 TeV from the region due to bremsstrahlung emission; (7) the total power from the synchrotron-radiating electrons into all loss processes (ionization, bremsstrahlung, inverse Compton emission, synchrotron emission).

## 9.9 Conclusions

This chapter has outlined the main arguments which point to vastly different GC magnetic field amplitudes with over two orders-of-magnitude difference. The arguments for a new way of distinguishing between the two values, in terms of the presence of a “spectral break”

in the GHz frequency radio continuum spectrum was explored via the changing of dominant cooling mechanisms from synchrotron emission at higher frequencies, to bremsstrahlung, were outlined. The spectrum of a region of bright synchrotron emission known as the DNS discovered by LaRosa et al (2005) was extended from 330 MHz up to 14.35 GHz, with a non-thermal spectrum being present to frequencies of at least 10 GHz without the subtraction of the relevant background emission. This chapter has outlined two methods by which the subtraction of the small scale emission within the DNS was subtracted (in addition to the GSB subtraction), of which Fourier analysis was determined to be the most robust method (as opposed to unsharp masking).

After subtraction of the appropriate background emission, the integrated flux density of the DNS was found to have a spectral break at a frequency of $\sim 1.6$ GHz of $\sim 0.6$, where through spectral fitting, the null hypothesis – of a single power-law describing the spectrum – can be excluded at very high confidence, strongly suggesting the presence of a spectral break.

The presence of a break however, does not in itself allow the determination of the magnetic field amplitude of the DNS. In addition to the radio continuum spectrum, this chapter has suggested that VHE $\gamma$-ray observations of EGRET and HESS at GeV and TeV energies respectively, place strict limits on the emissivity of DNS $\gamma$-ray photons that place a lower limit of the magnetic field amplitude for the DNS of $\gtrsim 100\,\mu$G. Further evidence, not only that the magnetic field amplitude has a lower limit at this value, but that the actual value lies close to $100\,\mu$G is outlined in Crocker et al. (2009). In any case, the evidence presented in this chapter indicates that the magnetic field in the GC region plays an important role in stellar dynamics – something that is not the case if the magnetic field amplitude is as low as that argued by LaRosa et al (2005).

# 10 Further Work and Conclusions

## 10.1 Scope for further work

The spectacular explosion in the number of Galactic objects that exhibit emission up to energies of a terra-electron volt (TeV) detected by instruments such as the High Energy Stereoscopic System (HESS), illustrates that particle acceleration up to energies >100 TeV (such as in RX J1713.7-3946) can occur in Galactic objects. Typically it is thought that shell-type supernova remnants (SNRs) should be the dominant sites of Galactic cosmic-ray (CR) acceleration up to $\sim 10^{15}$ eV (Ginzburg, 1964), where CRs (both hadrons and electrons) are injected into SNR shock fronts and accelerated through diffusive shock acceleration. $\gamma$-rays can then be produced through the interaction of the CRs with ambient molecular matter and/or electromagnetic fields. The observation of $\gamma$-rays from a SNR however, is not conclusive evidence the SNRs can accelerate particles to this energy, since inverse Compton scattering from accelerated electrons at lower energies can also explain TeV emission from an SNR (Gabici et al, 2008).

Disentangling where, how and which type of particles are responsible for an observed $\gamma$-ray source is a difficult task. This task can be made easier by studying regions which contain a SNR which is adjacent to molecular material. Two regions which exhibit a promising molecular/$\gamma$-ray correlation and upon which the work presented in this thesis could be extended to are W 28 and RCW 106.

Photons at radio frequencies have energies of $\sim 10^{-5}$ eV – a staggering *15–20 orders-of-magnitude* less than the particles which create the $\gamma$-ray emission – however they offer information to improve upon distinctions between nucleonic and electronic scenarios that the $\gamma$-ray and molecular correlation alone cannot provide. There are two crucial pieces of information that radio emission can provide: spectral and morphological details. The spectral information contained in radio photons allows one to differentiate between non-thermal (such as synchrotron and inverse Compton) and thermal emission (such as bremsstrahlung and blackbody radiators), whilst the morphological information gives spatial information about the different emission processes which are present in a source.

The Galactic centre (GC) exhibits a good correlation between the $\gamma$-rays and the molecular matter (as shown in Figure 10.1), and this could be further exploited by extending the work presented in this thesis. The correlation is assumed to be evidence of the $\gamma$-ray emission tracing the interaction of the nucleonic component of the CR spectrum with the ambient molecular matter. Since in both cases (W28/RCW106 and the GC), a electronic scenario cannot be ruled out – a good correlation between molecular matter and $\gamma$-ray emission alone does not indicate nucleonic emission – it is important to use other wavebands

for further evidence of a electronic or nucleonic scenario.

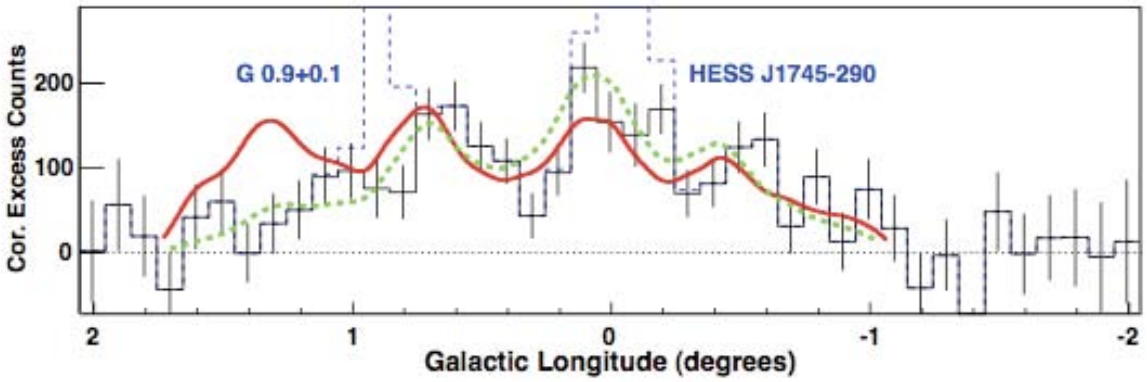


Figure 10.1: Excess count map for the GC region as observed with HESS from Aharonian et al (2006) as a function of Galactic longitude. The solid (red) line is the CS line emission (which traces the molecular matter), the solid (black) histogram with error-bars is the HESS TeV $\gamma$-rays after source subtraction (blue) dashed line shows the two point sources). Also shown is the expected excess counts for a point source model of proton diffusion occuring $10^4$-years ago as a (green) dotted line. It should be noted that the departure from the correlation at a Galactic longitude above $\sim 1^\circ$ can be explained with a single, central source, whereby particles from the central source have not diffused out to these longitudes.

Another example of the correlation of $\gamma$-rays with molecular material is W28 (of which several features are discussed in detail below), where molecular line information was used in concert with radio observations to enhance the prospect that the $\gamma$-ray emission of this source is due to nucleonic processes (Aharonian et al., 2008). Specifically, co-located molecular line and radio emission with a thermal spectral index of $\alpha \sim -0.2$ (i.e., a flux density following a power-law in frequency, such that $S_\nu \propto \nu^\alpha$, where $S_\nu$ is the flux density, $\nu$ is the frequency, and $\alpha$ is the spectral index) implies that the same population of electrons which is producing the thermal radio emission (through bremsstrahlung – though some synchrotron emission is possible – at $\sim$ GeV energies due to the decay chain and $N \rightarrow \pi^\pm \rightarrow e^\pm$. Here N is a hadron, $\pi^\pm$ are charged pions and $e^\pm$ are electrons and positrons) is also producing $\gamma$-rays (at $\sim$ TeV energies due to the decay chain $N \rightarrow \pi^0 \rightarrow 2\gamma$ for the $\gamma$-rays ) due to interactions of CRs with ambient matter. In order to further investigate the nature of the CR acceleration, it is essential to be able to distinguish between thermal and non-thermal emission processes at radio frequencies.

Furthering the work presented in this thesis could be done by exploring the three regions of Galactic $\gamma$-ray emission mentioned above, for which evidence exists of the interaction of CRs with the ambient molecular matter to attempt to discern between a nucleonic or electronic origin for the underlying CRs. These regions, the Galactic centre (GC), the giant molecular cloud (GMC) RCW 106, and W 28 are large molecular complexes which are known to have $\gamma$-ray emission either associated with (GC and W 28) or close-by (RCW 106).

In particular, investigation of the three sources could proceed in the following way:

1. There is a wealth of observational data available for the GC region at radio, infra-red, x-ray and $\gamma$-ray wavelengths. The correlation of the emission from the GC region at these wavelengths in order to attempt to elucidate how particles are accelerated and interact with the molecular environment in this complex region could be explored.

2. RCW 106 presents an excellent opportunity to explore the nucleonic scenario of CR

acceleration. This GMC is located (i) near to the unidentified HESS source HESS J1616-508, and (ii) close to a shell-like SNR, RCW 103, so that illumination of the cloud can be studied. In particular, the $\gamma$-ray (GeV-TeV) emission from this cloud, and the possibility of whether an observable excess of radio emission could be present from the electrons and positrons created in the nucleonic interactions could be investigated. This work will also be able to predict if the recently launched Fermi $\gamma$-ray telescope could observe an excess in the direction of this cloud.

3. W28 was recently discovered as a complex TeV $\gamma$-ray source by HESS, where a mixed-morphology SNR (W28) was found to be interacting with molecular clouds. Additionally this source (W28) is also a EGRET source at GeV $\gamma$-rays – making W28 one of only a few TeV sources for which there are currently GeV counterparts (Funk et al., 2008). Thus this source presents a unique opportunity to explore the possibility of synchrotron emission from secondary electrons and positrons created when CRs (such as protons which could be accelerated in the SNR) interact with the molecular clouds at GeV-TeV energies. Using radio recombination line and radio continuum data, the possibility of separating the thermal/non-thermal radio emission in the search for evidence of additional (to that from the SNR) non-thermal emission associated with the molecular material could also be explored.

Exploration of the possible correlation of the GC emission in the following key wavebands and the reasons for this could be used as follows:

1. Radio continuum maps from single dish and interferometric observations at as many frequencies between 300 MHz and 10 GHz. As was shown in Crocker et al. (2008), non-thermal radio emission can be observed up to at least 10 GHz from the GC region. Above these frequencies (and peaking at around 40 GHz), thermal emission from dust dominates the spectral energy distribution from this region. Thus the optimal frequency range with which to be sensitive to non-thermal emission and be able to separate this from non-thermal emission is thus in the 0.3–10 GHz range (below this absorption due to intervening HII regions absorbs any emission making an estimate of the true flux density extremely difficult at best). The addition of radio interferometric observations, such as that shown in Figure 10.2 at 1.4 GHz, allows the contribution of various background emission sources (such as the Galactic synchrotron background and extra-galactic sources) to be systematically taken into account.

2. FIR maps of the GC region, such as those freely available from the MSX and Spitzer space telescopes, can be used to distinguish between sources of thermal and non-thermal emission in the GC region. Gray (1994a) used the ratio of the 60 $\mu$m to 843 MHz Molongolo Observatory Synthesis Telescope emission to attempt separation of the thermal and non-thermal emission in the GC region, based on the work of Broadbent et al. (1989). This allows a systematic search along with other discriminators (such as polarization), of the parameter space of thermal/non-thermal emission to be carried out, increasing the accuracy of comparison with model $\gamma$-ray emission discussed below.

3. Molecular line emission (such as the CS line shown in Figure 10.1) traces the density and temperature of gas and provide a wealth of information for the discrimination of both thermal/non-thermal emission and target material for nucleonic interactions

producing the $\gamma$-ray and radio continuum emission. Exploration of not only the integrated emission, but that at different velocities will provide much additional information on the nature of the $\gamma$-ray emission.

4. The HESS (and now Fermi) telescopes have (and will) survey the GC at GeV–TeV energies, which cover the energy ranges producing TeV $\gamma$-rays and radio continuum emission. Thus integral to this project is the availability of the highest sensitivity data at $\gamma$-ray energies.

Using the data stated above, An investigate the origin of the $\gamma$-ray emission could proceed in a number of ways:

1. Direct comparison. As shown in Figure 10.1, and further illustrated in Aharonian et al (2006), there is a good correlation from comparison with CS emission, however, this has not been undertaken statistically. Using CS, and other maps obtained with the Mopra telescope, would allow an investigation of how statistically significant the correlation is using a method such as the maximum likelihood estimation method. This will allow a repeat analysis of Aharonian et al (2006), the result being a quantifiable measurement of how well the molecular matter in the GC correlates with the TeV $\gamma$-ray emission.

2. Using the FIR and radio continuum images, a model of the GC emission in terms of thermal and non-thermal emission could be produced. Specifically, the 2.4 GHz/60 $\mu$m correlation can be explored and the statistical correlation with the TeV $\gamma$-ray emission obtained as a function of position in the GC.

3. The information obtained from the correlation studies between radio, FIR and $\gamma$-ray images can then be compared to models of (i) CR penetration into clouds in areas where the above-mentioned correlations imply a nucleonic mechanism for $\gamma$-ray emission and (ii) $\gamma$-ray emission for the GC as a whole, such as that used in Wommer, Melia & Fatuzzo (2008).

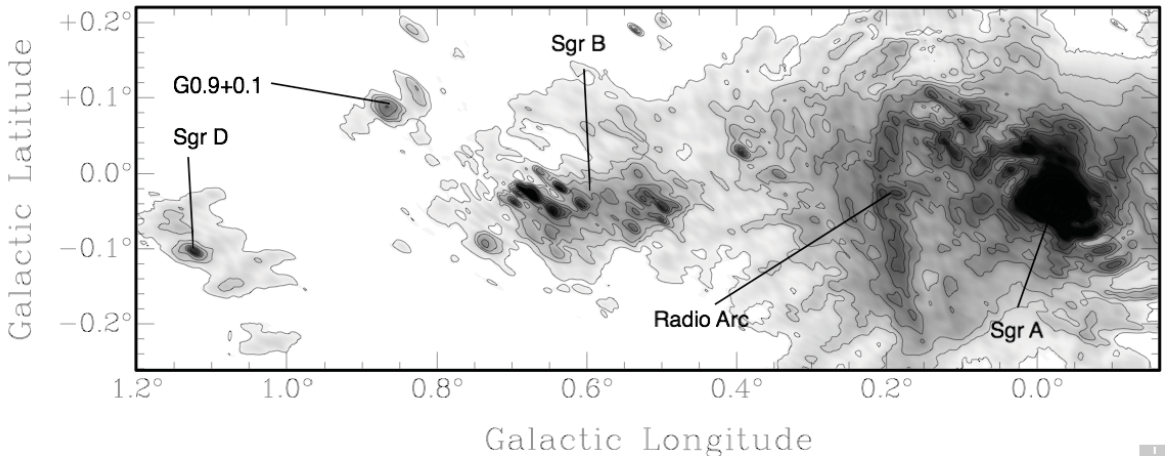


Figure 10.2: The centre of the Galaxy at 1384 MHz (Top) at a resolutions of 47″ × 18″ imaged with the Australia Telescope Compact Array (ATCA) Jones et al (2008a) with contours at: 0.1, 0.15, 0.2, 0.3, 0.4, 0.5, 0.6, 0.8, 1.6, 2.4, 3, 4, 5, 6, and 7 Jy per beam.

### 10.1.1 Tests of CR diffusion near HESS J1616-508

HESS J1616-508 is an unidentified extended TeV $\gamma$-ray source discovered in the HESS Galactic plane survey located, in projection, between two known SNRs, including RCW 103 and several nearby pulsars. There is, however, a large complex of molecular material, known as RCW 106 which is – assuming that the $\gamma$-ray and molecular material are at the same distance – at a projected distance of $\sim$ 40 pc. This provides an opportunity to explore the interaction of a $\gamma$-ray source with a large complex of molecular material where the source and target are clearly defined, and provided the distances between the sources are not prohibitive (i.e. $\lesssim$ 100 pc; Gabici & Aharonian 2007) in order to model the broadband spectrum.

The hypothesis is that CRs are accelerated in the HESS J1616-508 source, which then diffuse away from the source towards (not preferentially) the RCW 106 cloud. Information about the CR spectrum in this region can be obtained through the correlation of the $\gamma$-ray emission with molecular matter. Although the lack of strong radio continuum emission indicates that there is probably not much molecular material associated with this source, to date there has not been a published study on the molecular emission from this region in respect to the recently discovered $\gamma$-ray source. To establish the possibility (or lack thereof) of a nucleonic origin to the $\gamma$-ray emission from the HESS J1616-508 source, the distribution of molecular emission in the vicinity of the HESS J1616-508 source could be explored.

If a correlation of the TeV $\gamma$-ray emission and molecular material – which is at a distance which is consistent with the bulk of the RCW 106 emission – exists, the information about the CR spectrum thus could provide evidence to explore the expected broadband emission of RCW 106 GMC from radio continuum emission (including synchrotron emission from secondary particles) to TeV $\gamma$-rays . The expected emission from TeV $\gamma$-rays could then be searched for in the data from the HESS Galactic plane survey and lead to future proposals to use the HESS telescope to search for such emission.

To attempt to predict broadband emission from radio to $\gamma$-rays from RCW 106, the expected radio emission could be modelled using an estimate for the magnetic field structure and amplitude (provided by FIR polarization emission studies (Li et al., 2006) and the magnetic field - density relation (Crutcher, 1999) respectively) of RCW 106. This can then be compared with radio continuum emission observed at 1.4 and 2.4 GHz with ATCA presented in this thesis to provide a constraint on the magnetic field from this cloud – this was explored in Jones et al (2008a) on a smaller scale, and can be expanded to include the cloud as a whole.

### 10.1.2 Possible nucleonic origin of $\gamma$-rays in W28

The discovery paper of TeV $\gamma$-rays in W28 (Aharonian et al., 2008) explored the origin of the GeV and TeV $\gamma$-rays using a broadband approach. In particular, the TeV $\gamma$-rays were observed to correlate well with not only the large shell-like SNR, but also three other sources nearby, labelled as HESS J1800-240A,B and C. Interestingly, whilst HESS J1800-240C is a possible SNR, the brighter parts of this new source correlated well with $^{12}$CO(J=1-0) observations from the NANTEN telescope. It is stated that the distance to the molecular emission is unknown, however, this correlation points towards a possible nucleonic scenario of this source.

The possibility of accurately modeling the thermal radio continuum emission from these molecular regions could be explored in an attempt to investigate the possibility

of non-thermal synchrotron emission from secondary (or primary) electrons which are created concomitantly with the $\gamma$-rays in a nucleonic scenario for the $\gamma$-ray production. A positive result is significant as it gives us important information about the CR spectrum and magnetic field amplitude.

In order to do this, archival radio recombination line (RRL) emission observations either from the VLA or the ATCA could be searched for. A positive detection of RRL emission would allow the measurement of the conditions of thermal emission from the region to be established. This can then be used, in concert with the continuum emission at these frequencies to obtain information about the size of these regions to accurately model the thermal emission from the region. With sensitive enough radio observations ($\sim$ 1 mJy RMS noise), a search for an excess in emission at low radio frequencies $\lesssim$ 1 GHz, which could contain spectral information may be possible. Finally, using the information from molecular line emission, such as the NANTEN images, a mass and average ambient matter density for the regions could be obtained. Using the mass, density and low-frequency radio continuum emission information, an investigation the possibility that such emission could be due to the synchrotron emission from secondary electrons – possibly explaining the origin of the southern $\gamma$-ray emission regions – could be carried out.

## 10.2 Summary of main findings

This thesis has presented an exploration of the cosmic ray spectrum and the magnetic field amplitude at several positions within the Galaxy. This has been performed through the investigation of synchrotron emission due to the production of secondary electrons and positrons due to the interaction of cosmic ray hadrons with ambient nucleonic matter. The model for this emission is a simple one: a single-zone static model that has been applied in away from and towards the Galactic centre. Specifically, the main conclusions of this thesis can be divided into five categories: (i) upper limits to the magnetic field in cold, dark dense cores away from the GC; (ii) search for synchrotron emission from Sgr B2; (iii) observations of the GC at positive latitudes as a guide for later work to be applied to investigation of particle acceleration in the GC region; (iv) the serendipitous discovery of a SNR at the edge of the main complex of Sgr B2 cloud; and (v) the use of interferometric and single-dish observations in searching for – and finding evidence for – a spectral break in the DNS at the GC, which was then used to constrain the amplitude of the large-scale magnetic field at the GC. Below, we outline the major outcomes for each category.

### 10.2.1 Upper limits to the magnetic field in cold dark dense molecular cores

Chapter 5 reports on the search for synchrotron emission from molecular clouds due to the production of secondary electrons and positrons, which based on modeling of the spectrum (described in detail in Chapter 4) was predicted to have a $5\sigma$ detection at levels of $\sim$ 1 mJy. The two clouds chosen were the starless core, G333.125-0.562, and the molecular cloud IRAS 15596-5301. The results can be summarized as follows:

1. The observations of G333.125-0.562 were the first detailed images of this core to be published, with no evidence for radio emission down to a $1\sigma$ level of 0.5 mJy beam$^{-1}$ . Using published details on the mass and density of the core, we placed an upper limit on the magnetic field amplitude perpendicular to the line of sight of $B_{\perp} < 0.5$ mG.

2. We have extended the previous (published) observations of the molecular cloud IRAS15596-5301 down to 843 MHz. The radio continuum spectrum of this source is found to be that of optically thin free-free (bremsstrahlung) emission. We can place an upper limit on the magnetic field amplitude perpendicular to the line of sight of $B_\perp < 0.5$ mG based on the flux density required to significantly alter the spectrum at low frequencies away from that of an optically thin free-free HII region.

### 10.2.2 Search for synchrotron emission from Sgr B2

Chapter 6 is a paper which presents the first sensitive sub-arcminute images of the Sgr B2 region at 2.4 GHz and extends the search for synchrotron emission from Sgr B2 due to secondary electrons found in Protheroe et al. (2008). This was done by investigating the spectral and morphological evidence for synchrotron emission in both the total intensity and polarized emission from Sgr B2.

Specifically, Chapter 6 describes the process by which the spectrum used to constrain the diffusive transport suppression factor in Protheroe et al. (2008) was obtained. A further analysis of the data was performed by searching for polarized emission either (i) associated with the molecular matter in Sgr B2 as traced by the $NH_3$ emission or (ii) associated with the 'limb-brightened' effect predicted in Protheroe et al. (2008). No such polarized emission was observed and it was concluded that there is no evidence for polarized emission from Sgr B2.

Finally, the total intensity emission was used to searched for: (i) correlation with the $NH_3$ emission; (ii) evidence of 'limb-brightened' emission and; (iii) constrain the diffusive transport suppression factor. Although no evidence for synchrotron emission due to secondary (or primary) electrons was detected, it was possible to place upper limits to the diffusive transport suppression factors of GeV CRs into the Sgr B2 cloud to levels lower than $\chi < 0.01$ – an order of magnitude lower than that allowable from the integrated Sgr B2 radio continuum spectrum (i.e. Protheroe et al. (2008)).

### 10.2.3 Observations of the GC at 1384 and 2368 MHz with the ATCA

Chapter 7 presents an extension of the images for Sgr B2 presented in Chapter 6. These use the single-pointing and mosaic observations at 1384 and 2368 MHz obtained for the Sgr B2 observations and combines them with archival interferometric and single-dish observations of Sgr A. The resultant images are the first sub-arcminute images of the GC ever produced at 2.4 GHz and the sensitivity at 1.4 GHz matches previously published images of the GC. We used these images to catalogue the spectral and morphological structure of the major sources in the region, including Sgr A, Sgr B, Sgr D, G0.9+0.1, and the Radio Arc. The images presented in this chapter represent the first images of the Radio Arc at 2.4 GHz, and present a wonderfully complex morphology of the interaction between the Radio Arc and the ionized filaments. These images represent the first steps in a campaign to map the GC region at GHz wavelengths using either the upgraded ATCA or the eVLA (see Section 10.1 for example).

### 10.2.4 Discovery of a SNR at the edge of the Sgr B2 cloud

Chapter 8 examined closely the evidence for non-thermal radio continuum emission from a source located to the south of Sgr B2, which we dubbed the southern complex, or Sgr B2(SC).

This took the form of radio continuum observations with the ATCA and VLA between 0.3 and 8.6 GHz, which shows a non-thermal spectrum of $\alpha \sim -0.7$ between 1.4 and 2.4 GHz and $\alpha \sim -0.5$ between 2.4, 4.8 and 8.6 GHz. This spectrum – which we have shown can be explained using synchrotron emission – implies that the underlying spectrum of CR electrons has a spectral index of $\gamma = -2.4$ and is strongly suggestive of particles accelerated in shocks, such as those found in a SNR. This is reenforced by the radio continuum morphology, which shows that there is a shell-like morphology and – for the first time at 1720 MHz – an extension towards the east. We used archival 1720 MHz observations to search for, but failed to find, OH maser emission which has been strongly associated with shocked material in objects such as SNRs. The environment in which this source is located however, suggests that the lack of OH maser emission does not rule out an object with shocks, such as an SNR.

The extension towards the east is coincident with an X-ray source which we discovered in archival *XMM-Newton* 51 ks observations. This source has several features common to Galactic SNRs, such as the presence of the 6.7 keV Fe line, and the 1.8 keV Si line. Additionally, spectral fitting of the X-ray data shows that this source has a two plasma components – a 8 keV component consistent with the background Sgr B2 component – and an additional 0.15 keV component for which the spectral fitting of a SNR shock model produces features which are common to SNRs near the Galactic centre.

Although there is no spatial coincidence with the X-ray and radio (shell-like) source, we argued that on the basis of $NH_3$ observations that these objects are related, and the X-ray source represents the emission from the SNR shock which is expanding into a lower density region that that found at the position of the radio continuum source. The evidence for this is from high-resolution $NH_3$ observations, there is evidence for expanding shells at the position of the radio continuum source, which has been attributed to WR-stars on the basis of the energetics of the shells. We argue that because low-resolution $NH_3$ observations show that this source is very dense ($\sim 10^5$ cm$^{-3}$ ), that the energy estimated within the shell is a lower limit, and that because we observe a high density gradient towards the X-ray source, the SNR shell is expanding towards this region.

In totality, we suggest that the shell-like non-thermal nature of the radio-continuum source and the discovery of the X-ray source located precisely in the position of greatest density gradient away from this source is a new SNR. We suggest that this SNR has exploded in or near the edge of the envelope of Sgr B2 about 3000 years ago, and the shock has produced a shell like morphology which is observed in radio and $NH_3$ line emission. The large density gradient and high column density towards this region imply that the X-ray source is only bright where the shock has expanded into lower density region.

### 10.2.5 The large-scale magnetic field amplitude in the Galactic Centre region

Chapter 9 represents a major conclusion about the magnetic field amplitude of the GC region and shows the power of exploring the radio spectrum and its connection with the $\gamma$-ray spectrum – despite their apparent 15–20 *orders-of-magnitude* difference in energy. It produces new evidence to solve a 20 year-old problem of the magnetic field amplitude at the GC, which shows contradictory evidence for amplitudes which are two orders-of-magnitude different (viz. 10 $\mu$G versus 1 mG).

Using an assemblage of single-dish observations of the GC region, we have searched for evidence of a spectral break in the radio continuum emission of the DNS. Evidence of a break at GHz frequencies gives information about the conditions that the radiating electrons

(primary or secondary) find themselves in. Specifically, Chapter 9 shows that the frequency at which a spectral break is found is a function of the magnetic field amplitude and the ambient matter density because (i) synchrotron losses are dominated by the magnetic field and (ii) bremsstrahlung losses are dominated by the ambient matter density.

In order to show that this break is statistically significant, a number of background emissions were required to be subtracted from the radio data. Chapter 9 illustrates two methods for the subtraction of these backgrounds: Fourier analysis and unsharp masking. Both of these methods have never before been applied to such a problem.

Using the radio continuum spectrum to obtain an estimate for the conditions of the magnetic field amplitude and ambient density of the synchrotron emitting electrons, we have constrained the magnetic field amplitude on large scales to $> 100\,\mu$G due to values lower than this over-producing GeV and TeV $\gamma$-rays – in conflict with the EGRET and HESS limits for this region.

# Bibliography


Abraham, J., Abreu, P., Aglietta, M., et al., Science, 2007, 318, 896 - 897. 3, 4, 6

Abraham, J., Abreu, P., Aglietta, M., et al., Phys.Rev.Lett.101:061101,2008. 4

Aharonian, F., et al., 1997, Phys. Rev. Lett., 221, 102. 13

Aharonian, F., et al, 2004, A&A, 425, L13-L17. 11, 12

Aharonian, F. & Neronov, 2005, ApJ, 619, 306. 9, 13, 91

Aharonian, F., et al, Nature, 439, 2006. 12, 70, 74, 98, 117, 132, 134

Aitken, D. K., Greaves, J., Chrysostomou, A., et al. 2001, ApJL, 534, 173-177. 9

Akabane, K., Sofue, Y., Hirabayashi, H., Morimoto, M., Inoue, M. 1988, PASJ, 40, 459. 98

J. Albert, et al., 2006, Astrophys. J. 638, L101-L104. 11

Atoyan & Dermer, 2004, ApJ, 617, 123. 13

Baade, W., & Zwicky, F., 1934, PNAS, 20, 259. 5

Baganoff, F. K., Maeda, Y., Morris, M., et al, 2003, ApJ, 591, 891-915. 8, 9, 10, 11

Balick, B., & Brown, R.L., 1974, ApJ, 194, 265. 8

Beck, R., 2008, arXiv:0810.2923v1. 16, 17

Belanger, G., Goldwurm, A., Goldoni, P., et al., 2004, ApJL, 601, 163. 11

Bieging, J., Downes, D., Wilson, T.L., et al, A&AS, 42, 163, 1980. 70

Borkowski et al., 2001, ApJ, 548, 820. 105

Bower, G. C., Falcke, H., & Backer, D. C., ApJL, 523, 29-33. 8

Bower, G. C., Wright, M. C. H., Falcke, H, et al., 2001, ApJL, 2001, 555, 103-107. 8

Bower, G.C., Falcke, H., Sault, R. J., & Backer, D. C., 2002, ApJ, 571, 843. 8

Bridle, A. H. 1967, Mon. Not. Roy. Astron. Soc., 136, 219 117

Broadbent, A., Haslam, C. G. T., Osborne, J. L., 1989, MNRAS, 237, 381. 133

Brogan, C. L., Nord, M., Kassim, N., Lazio, J., & Anantharamaiah, K. 2003, Astronomische Nachrichten Supplement, 324, 17. 67

Brown, J.C., Haverkorn, M., Gaensler, B.M., et al., 2007, ApJ, 663, 258-266. 17

Cooper, B & Price, M, 1964, IAU Symposium No. 20, *The Galaxy and the Magellenic Clouds*, 20, 168. 98

Crocker, R. M., Jones, D., Protheroe, R. J., Ott, J., Ekers, R., Melia, F., Stanev, T., & Green, A. 2007, ApJ, 666, 934. 10, 49, 55, 70, 98, 126

Crocker, R.M., Jones, D.I., Melia, F., Ott, J., Protheroe, R.J., Nature submitted. 113, 133

Crocker, R.M., Jones, D.I., Melia, F., In preparation. 130

Crutcher, R. M., 1999, ApJ, 520, 706. 55, 56, 57, 62, 63, 135

Crutcher, R.M., in *Magnetic Fields in the Non-Masing ISM*, eds. J.M. Chapman & W.A. Baan, Cambridge Univ. Press, Cambridge, 2007, pp. 47-54. 16

Dickey, J.M., McClure-Griffiths, N.M., Stanimirovic, S., et al., 2001, ApJ, 561, 264. 121

Dowell, C.D., 1997, ApJ, 487, 237-247. 74

Downes, Goss, W.M., Schwartz, et al, A&AS, 35, 1, 1979. 73

Dubner, G., Giacani, E., & Decourchelle, A., astro-ph/0806.2777v1. 91, 92, 93

Duncan, A.R., Stewart, R.T., Haynes, R.F., et al, 1995, MNRAS, 277, 36. 67, 69, 84, 85, 87, 117, 120, 127

Ekers, R. D. & Rots, A. H., 1979 in Image Formation from Coherence Functions in Astronomy,

ed. C. van Schooneveld (Dordrecht: Reidel), 61. 74
Fermi, E.: Phys. Rev. 75, 1169, 1949. 43
Finkbeiner, D. P. et al. 2004, Astrophys. J., 617, 350. 127
Funk, S., Reimer, O., Torres, D. F. & Hinton, J. A., 2008, ApJ, 679,1299. 133
Gabici, S., & Aharonian, F., 2007, ApJ, 665, L131. 135
Gabici, S., arXiv:0811.0836v1. 5, 131
Gabici, S., Aharonian, F. A., & Blasi, P. 2007, APSS, 309, 365. 80
Gabici, S., Casanova, S., & Aharonian, F.A., arXiv:/0810.0035v1 5, 131
Gaensler, B.M., Pivovaroff, M.J., & Garmire, G.P., ApJ, 556, L107. 92
B.M. Gaensler, G.J. Madsen, S. Chatterjee, & S.A. Mao, 2008, PASA, 25, 184-200. 3
Garay, G., Brooks, K. J., Mardonnes, D., *et al.*, 2002, ApJ 579, 678-687. 56, 59, 61, 63
Garay, G., Faundez, S., Mardonnes, D, *et al.*, 2004, ApJ 610, 313-319. 55, 56, 59, 60, 62
Gaume, R.A., Claussen, M.J. ApJ 103, 1990. 66, 70, 98
Gaume, R. A., Claussen, M. J., de Pree, C. G., Goss, W. M., & Mehringer, D. M. 1995, ApJ, 449, 663 73
Ginzburg, V.L., & Syrovatskii, S.I., in *The Origin of Cosmic Rays* New York: Macmillan, 1964. 1, 131
Gray, A.D., MNRAS, 270, 822-834, 1994. 73, 94, 98, 112, 133
Gray, A.D., MNRAS, 270,835-846, 1994. 94, 95
Green et al. 1997, AJ, 114, 2058. 111
Greisen, K., 1966, Phys. Rev Lett. 16, 748. 4
Handa, T., Sofue, Y., Nakai, N., et al., PASJ, 39, 709-753, 1987. 117, 127
Haslam, C. G. T.; Salter, C. J.; Stoffel, H.; Wilson, W. E., A&A Supplement Series, 47, 1982. 118, 125
Haynes, R.F., Stewart, R.T., Gray, A.D., et al., 1992, A&A, 264, 500-512. 126
Hietler, W., 1954 in *The Quantum Theory of Radiation*, pp. 204-211. Oxford: Clarendon Press. 33
Helfand, D.J., & Becker, R.H., 1987, ApJ, 314, 303. 91
Hillas, A.M., 1984, ARA&A, 22, 425-444. 3
J. A. Hinton, and F. A. Aharonian, 2007, AJ. 657, 302-307. 13
Inui, et al., 2008, arXiv/0803.1528. 111
Jones, D.I., Crocker, R.M., & Protheroe, R.J., 2008, PASA, 25, 161-165. 50
Jones, D.I., Crocker, R.M., Ott, J., et al. AJ submitted. 55, 62, 98, 119, 134, 135
Jones, D.I., Lazedíc, J.S., Crocker, R.M., et al, in preparation. 73, 120
K. Kosack, et al., 2004, Astrophys. J. 608, L97-L100. 11
Koyama, K., Maeda, Y., Sonobe, T., et al., 1996, PASJ, 48, 249. 11, 104
Koyama, K., Inui, T., Hyodo, Y., et al., 2007, PASJ, 59, S221. 109, 110
Koyama et al. 2007, PASJ, 59, S245 104
Lang, C., Palmer, P., Goss, W.M., astro-ph/0801.2168. 66, 70, 98
Langston, G. et al., 2000, AJ, 119, 2801. 117, 127
LaRosa, T. N., Kassim, Namir E., Lazio, T. Joseph W., Hyman, S. D., AJ, 119, 207-40, 2000. 7, 66, 67, 68, 73, 82, 87, 91, 93, 98, 118, 119, 120
LaRosa, T. N., Kassim, N. E., Lazio, T. J. W., & Hyman, S. D. *The Universe at Low Radio Frequencies*, Proceedings of IAU Symposium 199, held 30 Nov - 4 Dec 1999, Pune, India. Edited by A. Pramesh Rao, G. Swarup, and Gopal-Krishna, 2002., p.268. 100, 102
LaRosa, T.N., Nord, M.E., Lazio, T.J.W. & Kassim, N.E., 2003, ApJ, 607, 302-308. 74
LaRosa, T.N., Brogan, C.L., Shore, S.N., et al., ApJL 626, 2005. v, 113, 114, 117, 118, 119, 121,

122, 125, 127, 130
Launhardt, R., Zylka, R., & Mezger, P. G. 2002, Astron. Astrophys., 384, 112 127
Law, C.J., Yusef-Zadeh, F., Cotton, W.D., et al, astro-ph:0801.4294. 70, 89, 90, 110, 119, 125
Lazendic, J. S., Dickel, J. R., Haynes, R. F., et al., 2000, ApJ, 540, 808. 75
Lazendic, J. S., et al., 2005, ApJ, 618, 733. 106, 109
Li, H., Griffin, G.S., Krejny, M., et al., 2006, ApJ, 648, 340-354. 135
Lo, et al, MNRAS, 2007. 56, 63
Lockett, P., Gauthier, E., Elitzur, M., 1999, 511, 235-241. 111
Longair, M. S., *High Energy Astrophysics*, CUP, 1994. 1, 3, 4, 14, 16, 33, 35, 38, 43, 49
Lyndon-Bell, D., Rees, M. J., 1971, MNRAS, 152, 461. 8
Malin, D.F., & Zealey, W. J., 1979, Space & Telescope, 57, 354. 121
Martin et al., 2008, ApJ, 678, 245. 111
Martin-Pintado, J., Gaume, R. A., Rodríguez-Fernández, N., et al., 1999, ApJ, 519, 667. 106, 111, 112
Mauch, T., Murphy, T., Buttery, H.J., et al, 2003, MNRAS, 342, 1117-1130. 58, 60, 67
Mehringer, et al, ApJ, 401, 168, 1992. 66, 70, 71, 72, 100
Mehringer, et al, 1993, ApJ, 412, 684. 98, 100, 102, 104, 107, 111
Mehringer, D.M., Palmer, P. & Goss, W.M., ApJSS, 97; 497-511, 1995. 66, 70, 71, 73, 98
Mehringer, D.M., Goss, W.M., Lis, D.C., et al, ApJ, 493, 274-290, 1998. 93, 94, 95
Melia, F., & Falke, H., Ann. Rev. Astron. Astrophys., 39, 309-52, 2001. 7, 86
Meyer-Hasselwander, H.A., et al., 1998, A&A, 335, 161. 11, 128
Moffat, A. T. ,1975, in *Galaxies and the Universe: Stars and Stellar Systems, Vol. 9*, ed. A. Sandage, M. Sandage, & J. Kristian (Chicago: Univ. Chicago Press), 211. 114
Mori, M., 1997, ApJ, 478, 225. 51
Morris, M., & Serabyn, E. 1996, ARA&A, 34, 645 6, 115
Morris, M., & Yusef-Zadeh, F. 1989, Astrophys. J., 343, 703. 114
Morris, M., & Yusef-Zadeh, F., A.J., 90, 2511, 1984. 83
Morris, M. 2007, ArXiv Astrophysics e-prints, arXiv:astro-ph/0701050 128
Moskalenko, I. & Strong, A.,1998, ApJ,493,694. 51, 56
Muno et al., 2006, ApJS, 165, 173. 106, 110
Murakami, H., Koyama, K., Sakano, M., Tsujimoto, M., & Maeda, Y. 2000, ApJ, 534, 283 104
Murakami, H., Koyama, K., & Maeda, Y. 2001, ApJ, 558, 687 101, 104
Narayan, R., Mahadevan, R., Grindlay, J. E., et al., 1998, ApJ, 492, 554. 8
Nord, M.E., Lazio, T.J.W., Kassim, N.E., et al., AJ, 128, 1646-70, 2004. 8, 67, 108
Noutsos, A., Johnston, S., Kramer, M., & Karastergiou, A., 2008, MNRAS, 386, 1881-1896. 17
Novak, G., Dotson, J.L., Dowell, C.D., et al, 1997, ApJ, 487, 320. 74
Odenwald, S.F., in I.A.U. Symp. 136, The Center of the Galaxy, ed. M. Morris (Dordrecht: Kluwer), 205, 1989. 94
Ott, J., Weiss, A., Staveley-Smith, L., & Henkel, C. 2006, Bulletin of the American Astronomical Society, 38, 920 67, 73, 76
Quataert & Loeb 2005, ApJ, 635, 45. 13
Pedlar, A., Anantharamaiah, K.R., Ekers, R.D., et al, 1989, ApJ 342,769-784. 10, 83, 85, 86, 87, 88, 89, 90, 95
Platania, P.et al. 2003, A&A, 410, 847. 118
Pohl, M. 2005, Astrophys. J., 626, 174. 11, 128
Predehl, P, & Schmitt, J. H. M. M., 1995, A&A, 293, 889. 7
Protheroe, R.J., & Clay, R. W., 2004, PASA, 21, 1-22. 3, 4, 6

Protheroe, R.J., 2004, APh, 21, 415-431. 3
Protheroe, R.J., Ott, J., Ekers, R.D., et al, 2008, MNRAS, 390, 683. 66, 73, 74, 76, 78, 80, 81, 82, 109, 137
Qin, S.-L., Zhao, J.-H., Moran, J. M., Marrone, D., Patel, N., Liu, S.-Y., Kuan, Y.-J., & Wang, J.-J. 2006, Journal of Physics Conference Series, 54, 468 67, 77
Raymond et al., 1977, ApJSS, 35, 1977, 419. 105
Reich, W., Fuerst. E., Steffen, P., Reif, K., Haslam, C.G.T. 1984, A&A, Suppl., 58, 197-248 117, 127
Reich, P., & Reich, W., A&A Supplement Series, 63, 205-288, 1986. 67, 69, 84, 85, 90
Reich, W., Reich, P., Fuerst, E., 1990, A&A, Suppl.,83, 539-568 117, 127
Aharonian et al., 2008, A&A, 481, 401-410. 132, 135
Roy, S., & Rao, A.P., 2006, JPhCS, 54, 156-160. 8
George B. Rybicki, Alan P. Lightman, 1979,"Radiative Processes in Astrophysics" (John Wiley & Sons: New York) . 43, 57, 74
Sakano et al. 2004, MNRAS, 350,129. 110
Sault, R. J., & Kileen, N., Miriad Users Guide, ATNF. 30
Sault, R. J., & Macquart, J. P., 1999, ApJL, 526, 85-59. 8, 74, 75
Sault, R.J., Bock, D.C.-J., & Duncan, A.R., 1999, A&ASS, 139, 387. 8, 74, 75
Sawada, M., Tsujimoto, M., Koyama, K., et al, astro-ph/0805.2079v1. 93
Schmidt, J. 1978, PhD dissertation, University of Bonn. 119
Slysh, V.I., Val'tts, I.E., Kalenskii, S.V., et al, A&AA, 134, 115-128, 1999. 73
Sofue, Y., & Reich, W. 1979, Astron. Astrophys. Supp., 38, 251 119, 121, 123
Sofue, Y., Takahara, F., Hirabayashi, H., et al., 1983, PASJ, 35, 437-445. 126
Stanimirovic, S., *ASP Conference Series: Single-Dish Radio Astronomy: Techniques and Applications*, Eds. Stanimirovic, S., Altschuler, D.R., Goldsmith, P.F. & Salter, C.J.,Vol. 278, 2002. 24, 30, 69, 119
X. H. Sun, W. Reich, A. Waelkens, and T. A. En$\beta$lin, A&A 477, 573-592 (2008). 17, 18
Takagi, S., Murakami, H. & Koyama, K., 2002, ApJ, 573, 275. 101, 105, 110
*Synthesis Imaging in Radio Astronomy II*, ASP Conference Series, Vol. 180, 1999. Eds. Taylor, G.B., Carilli, C.L. & Perley, R.A. 19
Thompson, T. A., Quataert, E., Waxman, E., Murray, N., & Martin, C. L. 2006, Astrophys. J., 645, 186 17
Tsuboi, M., Inoue, M., Handa, T., et al., 1986, AJ, 92, 818. 114, 115
Tsuchiya et al., 2004, Astrophys. J. 606, L115-L118. 11
Val'tts, I.E., Ellingsen, S., et al, MNRAS, 310, 1077, 1999. 73
van Eldik, E., arXiv:0811.0931, 2008. 8, 13
Voelk, H. J. 1989, Astron. Astrophys., 218, 67. 118
Völk,m H. J. & Bernlör, K., arXiv:0812.4198. 33, 35, 36, 38, 39, 41
Q. D. Wang, F. J. Lu, and E. V. Gotthelf, MNRAS, 2006 367, 937-944. 13
Wardle, M., 1999, ApJL, 525, L101. 111
Weekes, T.C., et al., 1989, ApJ 342, 379. 38
Whiteoak & Gardner 1976 , MNRAS, 174, 627. 103
Wommer, E., Melia, F., & Fatuzzo, M. 2008, Mon. Not. Roy. Astron. Soc., 387, 987 134
Yusef-Zadeh, F., Morris, M., & Chance, D., Nature, 310, 557, 1984. 89, 90
Yusef-Zadeh, F., Morris, M, 1987,ApJ, 320, 545-561. 85, 114
Yusef-Zadeh, F., Morris, M., 1987, AJ, 94, 1178. 89
Yusef-Zadeh, F., Melia, F., & Wardle, M., 2000, Science, 287, 85. 9, 10

Yusef-Zadeh, F., Hewitt, J.W. & Cotton, W., ApJS, 155, 421-550, 2004. 74, 85, 89, 90, 114
Zatsepin, G.T. & Kuzmin, V.A., Sov. Phys. JETP. Lett. 4, 78 (1966) 4